Modelling the dynamics of cold dark matter beyond shell crossing

Mandar Karandikar

Masterarbeit in Astrophysik
angefertigt im Argelander-Institut für Astronomie

vorgelegt der

Mathematisch-Naturwissenschaftlichen Fakultät der
Rheinischen Friedrich-Wilhelms-Universität Bonn

December 2020

I hereby declare that this thesis was formulated by myself and that no sources or tools other than those cited were used.

Bonn, 12/12/2020

Date

....

Signature

1. Thesis Advisor: Prof. Cristiano Porciani
2. First Examiner: Prof. Peter Schneider

Acknowledgements

I would like to thank my supervisor Prof. Cristiano Porciani for giving me the opportunity to work on this project, and for always being there to answer all of my questions. A lot of this work stems from our discussions, and I am grateful for his guidance along the way. I would also like to thank my second supervisor Prof. Peter Schneider for taking the time to read the thesis.

I also extend sincere thanks to Dr. Emilio-Romano Diaz for his help throughout the project, especially with running N-body simulations. Likewise, thanks to all the members of our research group for their encouragement and help.

This work would not have been possible but for the unwavering support of my friends in Bonn, who were a timely source of encouragement as well as distraction whenever I needed them.

This work uses the cosmological simulation code GADGET-2 [1]. The solvers are written in Python [2], which is also used for the analysis.

Contents

Introduction

The central problem of this work is the theoretical description of the dynamics of dark matter in an expanding universe, with regards to small-scale behaviour after different streams of matter have crossed each other. Through the course of this chapter, we set up the necessary cosmology, introduce the relevant terms, and make this problem precise by the end of the chapter.

We live in a Universe with a finite speed of light which appears to have had a beginning in time. Since our primary source of information about this Universe is electromagnetic radiation travelling at the speed of light, we can infer the presence of a cosmic horizon – a boundary of the observable Universe. The quantity that marks this boundary is the Hubble radius (R_H), and it is estimated to be about 14 Gpc. Within the observable Universe, the largest structures are walls and galaxy filaments, which have typical length scales of 70–120 Mpc, although a number of much larger structures have also been found. Galaxies (typically 10^3–10^5 pc) and galaxy clusters (typically 1–5 Mpc) reside within these filaments. The only fundamental force which operates on these scales is the gravitational force. Therefore, an attempt to understand the formation and evolution of structure on these scales has a natural starting point in a description of gravity.

It can be argued that Einstein's formulation of general relativity (GR) [3] – which remains our best theory of gravity – marks the beginning of modern Cosmology. GR posits that our Universe may be mathematically modelled by a four-dimensional pseudo-Riemannian manifold (spacetime) endowed with an intrinsic curvature. Then, gravity arises as a natural consequence of motion in curved spacetime. The theory is described by the Einstein field equation which characterises how matter and energy affect the curvature of spacetime, and the geodesic equation of motion which characterises the response of matter to this curvature. The field equation is the following equation for the metric tensor ($g_{\mu\nu}$) – an object which describes the notion of distance on the manifold

$$R_{\mu\nu} - \frac{1}{2}Rg_{\mu\nu} = \frac{8\pi G}{c^4}T_{\mu\nu} \,, \tag{1.1}$$

where $R_{\mu\nu}$ is the Ricci curvature tensor which describes deviations of the metric from Euclidean geometry, R is the Ricci scalar (scalar curvature) derivable from $R_{\mu\nu}$, and $T_{\mu\nu}$ is the stress-energy (or energy-momentum) tensor describing the matter density of the universe. The left side of the equation is often grouped together and the resulting tensor is called the Einstein tensor ($G_{\mu\nu}$).

Solutions of Eq. (1.1) can be written either by specifying the metric tensor explicitly, or by writing

an expression for the spacetime interval (ds^2) in terms of the metric

$$ds^2 = g_{\mu\nu}\, dx^\mu\, dx^\nu \ . \tag{1.2}$$

The solutions can be classified depending on an ansatz for the stress-energy tensor. The simplest model assumes that the tensor vanishes identically, which would be the case in the absence of matter and all non-gravitational fields. In this scenario, the manifold is Ricci-flat ($R_{\mu\nu} = 0$) and we have a trivial solution – the Minkowski metric – which combines the three-dimensional Euclidean space (x, y, z) with time t as a fourth dimension

$$ds^2_{\text{Minkowski}} = c^2\, dt^2 - (dx^2 + dy^2 + dz^2) \ . \tag{1.3}$$

The first nontrivial solution for the vacuum case appeared as early as 1916, proposed by Schwarzschild and independently by Droste [4, 5]. The Schwarzschild solution, as it is now known, describes the gravitational field outside a spherical mass. It can be proved that it is the most general spherically-symmetric solution in vacuum, and that there are no time-dependent solutions of this form (Jebsen-Birkhoff Theorem [6, 7]).

A class of cosmological solutions for homogeneous, isotropic, expanding spacetime was first derived by Friedmann (1922 – 1924) [8] and later independently by Lemaître [9]. Robertson and Walker (1935 – 1937) proved that this is the only solution on a homogeneous and isotropic spacetime [10–13]. The Friedmann–Lemaître–Robertson–Walker (FLRW) metric is given as

$$ds^2_{\text{FLRW}} = c^2\, dt^2 - a^2(t) \left\{ dr^2 + f_K^2(r) \left[d\theta^2 + \sin^2(\theta)\, d\phi^2 \right] \right\} \ , \tag{1.4}$$

where f_K is the curvature (K) dependent comoving angular diameter distance. For flat spacetime, $K = 0$, and $f_K(r) = r$ recovers the Minkowski metric in spherical coordinates with an additional time-dependent factor $a(t)$ multiplying the spatial coordinates. This scale factor encodes expansion of spacetime.

The FLRW metric is a good starting point in exploring simple but viable solutions of GR. There are three pieces of evidence which taken together suggest that the FLRW metric describes (at least to some degree) the real Universe. The first was the discovery of cosmic expansion by Hubble (1929) [14]. Hubble found that the galaxies were receding away with a velocity (v) proportional to their distance (d) from an observer on Earth,

$$v = H_0\, d \ , \tag{1.5}$$

where the proportionality constant H_0 is known as the Hubble constant, and describes the expansion rate of the Universe. It is conventionally expressed as

$$H_0 = 100\, h\, \text{km}\, \text{s}^{-1}\, \text{Mpc}^{-1} \ , \tag{1.6}$$

where h is a dimensionless parameter of order unity. It is useful to write distances in units of h^{-1} Mpc (or an appropriate length unit), and we shall follow this convention hereafter. The value of h is still a matter of some debate in the literature, with a statistically significant discrepancy in measurements from the local Universe (e.g. via the distance ladder) and the early Universe (e.g. from the cosmic microwave background) [15]. Lemaître had already pointed out that an expanding universe would have originated from a hot and dense early state. This has been subsequently called the 'Big Bang',

and is now the accepted cosmological model.

The second piece is the evidence for spatial homogeneity. This comes mainly from studies of the galaxy distribution via galaxy-redshift surveys, which show the absence of very large-scale structures. The first such survey was the CfA Redshift Survey [16], which found that the distribution is nearly homogeneous when averaged over large scales. This was corroborated to some extent by later surveys like the 2dF Galaxy Redshift Survey [17], and the Sloan Digital Sky Survey [18]. It appears that the Universe is mostly homogeneous on large scales, but is highly inhomogeneous on small scales, as evidenced by the observed galaxy clustering.

The final piece was the discovery that the cosmic microwave background (CMB) is highly isotropic, with temperature anisotropy of order 10^{-5}. The CMB is the left-over radiation from a hot early Universe. Its isotropy was observationally confirmed by the COBE satellite which mapped the CMB for the first time in 1992 [19]. Following satellites like *Planck* [20] have provided tighter constraints on the anisotropy. The isotropy of the CMB is suggestive of the isotropy of the early Universe. Making the Copernican assumption that our position in spacetime is not privileged, so that all freely-falling observers will measure this isotropy, we arrive at another argument for homogeneity – if space is isotropic everywhere, it is homogeneous. This class of freely-falling observers are called 'comoving', and the respective coordinates are called comoving coordinates[1] ($\mathbf{x}$). Comoving coordinates can be inferred in the expression for the metric, through the absence of cross terms like $dt\, dx^i$, e.g. in Eq. (1.4) (the matrix form of such a metric is diagonal).

Given the above results, the Ehlers-Geren-Sachs theorem guarantees that a universe in which all freely-falling observers measure the CMB as isotropic is described by the FLRW metric [21]. This has been generalised to imply that a universe which is *almost* isotropic can be described by a metric which is *almost* FLRW [22]. Given the FLRW metric, we can complete Eq. (1.1) by specifying $G_{\mu\nu}$ and $T_{\mu\nu}$, which will result in equations that describe the evolution of $a(t)$.

We begin this exercise by considering the matter-energy content of our Universe. The structure that we can directly observe on galactic scales is made of baryonic matter. Additionally, the Universe is populated by energy in the form of electromagnetic radiation. We can model this matter-energy pair with a perfect fluid. A perfect fluid is one without shear stress, anisotropic pressure, and viscosity. In the rest frame of the fluid, the stress-energy tensor then takes the following form

$$T_{\mu\nu} = \left(\rho + \frac{p}{c^2}\right) U_\mu U_\nu - p\, g_{\mu\nu} \,, \tag{1.7}$$

where ρ is the energy density of the fluid, and p is the isotropic pressure. Hereafter $g_{\mu\nu}$ is the FLRW metric unless specified otherwise. U_μ is the velocity four-vector, and takes the following form in the fluid rest frame

$$U^\mu = (c, 0, 0, 0) \,, \tag{1.8}$$

The stress-energy tensor is thus given by

$$T_{00} = \rho c^2 \,, \qquad T_{ii} = p a^2(t) \,. \tag{1.9}$$

Next, we turn to the Einstein tensor. The explicit calculation for $G_{\mu\nu}$ is long, therefore we relegate it

---

[1] The bold font indicates a vector quantity.

to Appendix A, and borrow the components of the Einstein tensor directly from Eq. (A.9),

$$G_{00} = -3\left(\frac{\dot{a}}{ac}\right)^2 , \qquad G_{ii} = \frac{2\ddot{a}a + \dot{a}^2}{c^2} . \tag{1.10}$$

Now we have all the pieces to return to Eq. (1.1)

$$G_{00} = -\frac{8\pi G}{c^4}T_{00} , \tag{1.11a}$$

$$G_{ii} = -\frac{8\pi G}{c^4}T_{ii} . \tag{1.11b}$$

Substituting the relevant quantities, we get the Einstein equations for a perfect fluid in a flat FLRW universe,

$$\left(\frac{\dot{a}}{a}\right)^2 = \frac{8\pi G\rho}{3} , \tag{1.12}$$

$$\frac{2\ddot{a}}{a} + \left(\frac{\dot{a}}{a}\right)^2 = -\frac{8\pi G p}{c^2} . \tag{1.13}$$

It is conventional to combine the above equations to get

$$\frac{\ddot{a}}{a} = -\frac{4\pi G}{3}\left(\rho + \frac{3p}{c^2}\right) . \tag{1.14}$$

Eq. (1.12, 1.14) together determine the evolution of $a(t)$, and are called the Friedmann equations.

Before we can solve the Friedmann equations, we need to determine how the fluid density and pressure evolve with the scale factor. To that end, we can enforce conservation laws. The conservation of energy and momentum means that the covariant derivative of the stress-energy tensor vanishes. The conservation of momentum ($\nabla_\nu T^{i\nu} = 0$) is already guaranteed by the translational invariance of the FLRW metric, and reveals no new information. The conservation of energy implies

$$\nabla_\nu T^{0\nu} = 0 , \tag{1.15}$$

or,

$$\frac{\partial\rho}{\partial t} + \frac{3\dot{a}}{a}\left(\frac{p}{c^2} + \rho\right) = 0 . \tag{1.16}$$

This equation admits a solution of the form $p = w\rho$. Substituting p in Eq. (1.16)

$$\frac{\dot{\rho}}{\rho} + 3(1 + w)\frac{\dot{a}}{a} = 0 . \tag{1.17}$$

For a constant w, this can be integrated to obtain an equation of state

$$\rho \propto a^{-3(1+w)} . \tag{1.18}$$

Different components of matter (energy) can be identified with different values of w. First, consider nonrelativistic pressureless matter often called 'dust' which makes up the ordinary stars and galaxies,

and for which $w = 0$. This leads to the following density dependence

$$\rho_m(t) \propto a^{-3}(t) , \tag{1.19}$$

which can be interpreted as the conservation of mass. As the universe expands, its volume grows as a^3, density as a^{-3}, keeping the mass constant. The next component is electromagnetic radiation, i.e., relativistic photons with $w = 1/3$. This gives

$$\rho_r(t) \propto a^{-4}(t) , \tag{1.20}$$

which is a combination of two effects. Expansion causes the energy density to fall as a^{-3}, and there is an additional fall $\propto a^{-1}$ due to Doppler redshift in an expanding universe.

In 1998, two groups of researchers working independently, measured the distances to type Ia supernovae. Comparing these measurements to the redshifts of these supernovae measured from their spectral lines, they could estimate how the expansion rate was changing with time. This led to the surprising discovery that the Universe was expanding at an accelerating rate [23, 24]. It is hypothesised that this is caused by the energy density of empty spacetime (called 'vacuum energy'), usually modelled as a perfect fluid with negative pressure, corresponding to $w = -1$. This could be interpreted as an additional term to Einstein's equation, and consequently the Friedmann equations. This term amounts to $\Lambda c^2/3$, where Λ is called the cosmological constant. However, Λ is easily absorbed in p or ρ, and is omitted from the equations. The vacuum energy density (ρ_Λ), being an intrinsic property of spacetime, is independent of expansion. Finally, we can write down the matter-energy density of our Universe as the sum of these three components,

$$\rho = \rho_m + \rho_r + \rho_\Lambda . \tag{1.21}$$

We can make the result more explicit by introducing proportionality constants $\rho_{c,0}$ for component c, which are the densities at the current epoch

$$\rho = \frac{\rho_{m,0}}{a^3} + \frac{\rho_{r,0}}{a^4} + \rho_\Lambda . \tag{1.22}$$

In the discussion so far, we have assumed the Universe to be flat. In general, a universe can either be flat ($K = 0$), open ($K > 0$), or closed ($K < 0$). We can use the first Friedmann equation (Eq. 1.12) to define the total energy density today for a flat universe, or the 'critical density' ρ_{cr}

$$\rho_{cr} := \frac{3H_0^2}{8\pi G} = \rho_0 . \tag{1.23}$$

We can use ρ_{cr} to scale our energy densities and obtain dimensionless density parameters

$$\Omega_m := \frac{\rho_{m,0}}{\rho_{cr}} , \qquad \Omega_r := \frac{\rho_{r,0}}{\rho_{cr}} , \qquad \Omega_\Lambda := \frac{\rho_\Lambda}{\rho_{cr}} . \tag{1.24}$$

The total density parameter today is then defined as

$$\Omega_0 = \Omega_m + \Omega_r + \Omega_\Lambda . \tag{1.25}$$

This parameter is measureable, and the measurements from *Planck* suggest that $\Omega_0 = 1.00 \pm 0.02$ [20]. Our Universe is almost exactly flat. We can now use Eq. (1.23–1.25) in the first Friedmann equation (Eq. 1.12) to obtain a useful relation

$$\left(\frac{H}{H_0}\right)^2 = \frac{\Omega_m}{a^3} + \frac{\Omega_r}{a^4} + \Omega_\Lambda \, , \tag{1.26}$$

where $H = \dot{a}/a$ is the Hubble function (the dot above a denotes a time derivative). Note that $a(t)$ is conventionally made dimensionless by setting $a(t_0) = 1$, and then scaling by it. We now have nearly all the pieces to complete the standard picture of Cosmology. The last piece is the most important one for this work, and concerns the measurement of Ω_m.

The traditional way of measuring Ω_m was to use the virial theorem to estimate the mass of a cluster of galaxies, calcuate an average ratio of mass to absolute luminosity (M/L), and use measurements of the total luminosity of the sky to estimate Ω_m. The assumption here is that the estimated mass-to-light ratio is representative of the Universe as a whole, and also that the target regions are virialised to an extent where deviations from the virial theorem are small. Our local neighbourhood – the Virgo cluster – does not fit these criteria, but others like the Coma cluster do. Using this method, Zwicky (1933) [25] realised that the mass-to-light ratio for the Coma cluster was much larger than the mass-to-light ratio of the visible parts of its component galaxies. A more recent study found $M/L = 348\,h\,M_\odot/L_\odot$ for 459 clusters ($M_\odot/L_\odot$ is the solar mass-to-light ratio) [26]. For elliptical galaxies, this number is closer to $20\,h\,M_\odot/L_\odot$ [27]. Since the cluster luminosity comes from its component galaxies, this discrepancy suggests that a large fraction of the galaxies' mass may be in the form of non-luminous matter.

In 1980, a study of the rotation curves of spiral galaxies revealed that their rotational velocities did not show a Keplerian decline ($v \propto r^{-1/2}$), but either remained flat, or exhibited a rising trend to large radii [28]. This indicates that the mass in these galaxies is not centrally concentrated, and extends out to radii much larger than the optical galaxy. The rotation curves are consistent with a spherical halo. Measurements of the dynamical mass of gravitationally lensed objects also reveals a similar discrepancy to their visible mass [29]. Further evidence for the existence of this 'dark' matter (DM) comes from estimates of the baryonic contribution to ρ_{cr}, which only amounts to $\approx 5\%$. DM must then be non-baryonic in nature (a summary of the different ways to measure Ω_m can be found in [30]). DM solves another problem related to structure formation. In the early universe, baryonic matter was coupled to radiation, and would not have had enough time to evolve into the structure we see today. DM is either always decoupled from radiation, or decouples much earlier than baryonic matter, allowing density perturbations to grow earlier.

Although there is substantial evidence for the existence of DM, its nature remains unclear. The candidates range from elementary particles like neutrinos and WIMPs (Weakly Interacting Massive Particles), light bosons like axions which have their origin in particle physics, and macroscopic candidates like primordial black holes. DM may be classified based on its velocity dispersion[2] compared to the expansion rate as 'hot', 'warm', or 'cold' [3]. Hot DM would be made of low mass ($10\,\mathrm{eV} < m < 100\,\mathrm{eV}$) ultrarelativistic particles like neutrinos, and in a universe dominated by hot DM the first structures to form would be superclusters of mass $10^{15}M_\odot$. The formation of smaller

---

[2] Another way to make this classification is using the free-streaming length λ_{fs}, e.g., [31].
[3] The free-streaming length is large for hot DM, and small for cold DM.

structures like galaxies in such a universe would be difficult to explain. Further, there is observational evidence that DM exists in dwarf spheroidal galaxies, providing a lower bound on the DM particle mass of $m > 500\,\text{eV}$, effectively ruling out Standard Model neutrinos. A warm DM dominated universe is slightly more plausible, where the intermediate mass ($\approx 1\,\text{keV}$) individual particles become nonrelativistic earlier than neutrinos. The first structures to form in such a universe would be typical galaxies of mass $10^{11}\text{M}_\odot$. However, our Universe is likely dominated by cold DM (CDM), which initially has a negligible velocity dispersion and negligible nongravitational interactions [32]. This would allow the DM particles to clump efficiently in the early universe. The assumption that velocity dispersion can be neglected holds in the linear regime of structure formation, especially on large scales. Here, the DM particles have a single coherent flow, and hence this is often called the single-stream approximation (SSA). As structure formation becomes nonlinear, this approximation breaks down with the generation of velocity dispersion and multiple streams. This is known as 'shell crossing' or 'orbit crossing'. In this work, we are interested in the theoretical treatment of DM dynamics in these multistreaming regions where the SSA no longer holds.

In summary, in the standard picture of cosmology – the ΛCDM model – the Universe is well-described by a flat ($\Omega_0 = 1$) spacetime dominated by vacuum energy ($\Omega_\Lambda \approx 0.7$), with baryonic ($\Omega_{\text{b}} \approx 0.04$) and non-baryonic ($\Omega_{\text{DM}} \approx 0.26$) matter making up the rest of the energy density. The mechanism of structure formation is the gravitational amplification of primordial fluctuations in a homogeneous background. Structure formation proceeds in a hierarchical manner, with small-scale structures forming first.

In the rest of this work, we study and compare theoretical methods that describe structure formation in a one-dimensional universe, with the goal of developing these methods before they can be applied to the full 3D problem. Although specialising from 3D to 1D represents a loss of information, there are still good reasons why an analysis of a 1D universe is interesting:

- The form of the equations we use is the same in 3D as in 1D (in fact, we will often derive the necessary equations in 3D)

- The high degree of symmetry in 1D makes the system simpler to solve

- There is an exact analytical solution until shell crossing in 1D, against which the performance of other methods can be judged

- The 1D model shares some features with its 3D counterpart, like coupling of large-scale modes, beat coupling, shifting and smearing of BAO peak, as described in [33]

We make two further simplifications. Firstly, since the scales involved in nonlinear collapse are much smaller than the Hubble radius, and the gravitational fields are weak, we can ignore relativistic corrections and use Newtonian gravity. Finally, we will assume a DM-only Einsten-de Sitter (EdS) universe [34], i.e., a universe without a cosmological constant ($\Omega_{\text{m}} = 1$, $\Omega_{\text{r}} = \Omega_\Lambda = 0$) as we are primarily interested in the gravitational interaction of DM. In such a universe, Eq. (1.26) simplifies to

$$H(t) = H_0 a^{-3/2}(t) \, , \tag{1.27}$$

which can be integrated with the initial condition $a(0) = 0$ to obtain the important result

$$a(t) = \left(\frac{3H_0 t}{2}\right)^{2/3} \, . \tag{1.28}$$

The rest of this work is structured as follows: in Chapter 2, we detail the theoretical methods used in this work, and arrive at the relevant equations that describe DM dynamics. We then describe the numerical solution of these equations in Chapter 3, followed by a discussion of the important results in Chapter 4. A summary is provided in Chapter 5, with comments on possible future work.

Theory

2.1 The Vlasov-Poisson System

To reiterate the central problem, we seek a theoretical description of DM dynamics in a 1D EdS universe with Newtonian gravity, focussing on the regime beyond shell crossing.

We start with N identical DM particles of mass m. In an expanding universe, the comoving coordinate $\mathbf{x}$ and the proper coordinate $\mathbf{r}$ are related as

$$\mathbf{r}(\mathbf{x}, t) = a(t)\mathbf{x} \ . \tag{2.1}$$

Differentiating with respect to the proper time t, we get

$$\mathbf{u}(\mathbf{x}, t) = \mathbf{v}(\mathbf{x}, t) + \frac{\mathrm{d}a(t)}{\mathrm{d}t}\mathbf{x} \ , \tag{2.2}$$

where

$$\mathbf{v}(\mathbf{x}, t) = a(t)\frac{\mathrm{d}\mathbf{x}}{\mathrm{d}t} \ , \tag{2.3}$$

is the peculiar velocity. It is related to the conjugate momentum $\mathbf{p}$ as

$$\mathbf{p}(\mathbf{x}, t) = a(t)m\mathbf{v}(\mathbf{x}, t) \ . \tag{2.4}$$

The only interaction that the DM particles have is due to the gravitational field described by the system. This can be written in the form of a smooth Newtonian comoving potential $\phi(\mathbf{x})$ related to the momentum via Newton's equation of motion

$$\frac{\mathrm{d}\mathbf{p}}{\mathrm{d}t} = -m\nabla\phi(\mathbf{x}) \ , \tag{2.5}$$

where the spatial derivative ∇ is with respect to $\mathbf{x}$.

The system is also characterised by a comoving mass density $\rho(\mathbf{x}, t)$. Here, we introduce the overdensity field (or density contrast) $\delta(\mathbf{x}, t)$ defined as

$$\delta(\mathbf{x}, t) = \frac{\rho(\mathbf{x}, t)}{\bar{\rho}(t)} - 1 \ , \tag{2.6}$$

where $\bar{\rho}(t)$ is the homogeneous background density at time t.

In the single-stream regime, the pair of fields $(\delta, \mathbf{v})$ describe the system of DM particles accurately. However, at shell crossing, the density contrast in a Lagrangian frame formally becomes singular, and the velocity field is no longer single-valued. We will formalise and discuss this issue in Section 2.2.

To capture the dynamics of the system at all scales and stages of evolution, we consider the following approach. Under the ΛCDM paradigm, the number of DM particles at the mean density of the Universe is extremely large even for the most massive candidates. For example, for WIMPs of mass 100 GeV, this number is[1] $\approx O(10^{80})$. In the limit of large N, two-body interactions are suppressed, and the system can be described as 'collisionless'. We are therefore modelling a classical system of indistinguishable, cold, collisionless DM particles. The system can thus be modelled statistically using a smooth distribution function $f(\mathbf{x}, \mathbf{p}, t)$ defined such that

$$f(\mathbf{x}, \mathbf{p}, t)\, \mathrm{d}^3\mathbf{x}\, \mathrm{d}^3\mathbf{p}$$

is the number of particles whose positions lie within a volume element $\mathrm{d}^3\mathbf{x}$ about $\mathbf{x}$ and momenta lie within a volume element $\mathrm{d}^3\mathbf{p}$ about $\mathbf{p}$. The distribution function is effectively a number density, and resides in the six-dimensional 'phase space' spanned by the comoving particle positions and their conjugate momenta. Each point $(\mathbf{x}, \mathbf{p})$ in phase space represents a state of the entire system. Since a scalar function completely describes its dynamics, this is a Hamiltonian system and follows Liouville's theorem, which states that 'the evolution of the distribution function along trajectories of the system in phase space is constant' [35]. The mathematical statement of Liouville's theorem is the collisionless Boltzmann (or Vlasov) equation

$$\frac{\mathrm{d}f}{\mathrm{d}t} := \frac{\partial f}{\partial t} + \frac{\mathrm{d}\mathbf{x}}{\mathrm{d}t} \cdot \frac{\partial f}{\partial \mathbf{x}} + \frac{\mathrm{d}\mathbf{p}}{\mathrm{d}t} \cdot \frac{\partial f}{\partial \mathbf{p}} = 0 \ . \tag{2.7}$$

Physically, this means that the system is incompressible in phase space.

To account for the self-gravity of the DM particles, we can use the Poisson equation for the potential $\phi(\mathbf{x})$ in an expanding background

$$\nabla^2 \phi(\mathbf{x}) = 4\pi G a^2(t) \left[\rho(\mathbf{x}) - \bar{\rho} \right] \ , \tag{2.8}$$

which can be written in terms of the overdensity using Eq. (2.6) as

$$\nabla^2 \phi(\mathbf{x}) = 4\pi G \bar{\rho} a^2(t) \delta(\mathbf{x}) \ . \tag{2.9}$$

The mass density $\rho(\mathbf{x})$ is the zeroth order momentum moment of the distribution given as

$$\rho(\mathbf{x}, t) = \int \mathrm{d}^3\mathbf{p}\, f(\mathbf{x}, \mathbf{p}, t) \ . \tag{2.10}$$

We can use this to obtain a coupled system of equations for the distribution function. Using Eq. (2.10)

---

[1] This is calculated by assuming a spherical universe of radius R_{H}, populated by identical DM particles of mass 100 GeV. Using the mean density of the universe today, we arrive at a total DM mass, and thus at a total particle number. This is meant to be a rough estimate of the typical number of particles involved.

in Eq. (2.9),

$$\nabla^2 \phi(\mathbf{x}) = 4\pi G \bar{\rho} a^2(t) \left[\int \mathrm{d}^3 \mathbf{p} \, f(\mathbf{x}, \mathbf{p}, t) - 1 \right] . \qquad (2.11)$$

To complete the coupling to the Poisson equation, we use Eq. (2.5) in Eq. (2.7), and rewrite the Vlasov equation as

$$\frac{\partial f}{\partial t} + \frac{\mathbf{p}}{ma^2} \cdot \frac{\partial f}{\partial \mathbf{x}} - m\nabla\phi \cdot \frac{\partial f}{\partial \mathbf{p}} = 0 . \qquad (2.12)$$

Eq. (2.11) and Eq. (2.12) together make up the Vlasov-Poisson (VP) system, which is a complete description of the time evolution of f in an expanding universe, with a gravitational potential sourced by f.

In the full 3D problem the VP equations are nonlinear, coupled, integro-differential equations in seven variables. Except for a few simple 1D cases, analytical solutions are nearly impossible, and the equations must be solved numerically for any realistic systems. This set of equations has a long history of numerical solutions, especially in plasma physics, where the only difference is a negative sign in the Poisson equation. In a cosmological setting, numerical simulations approximate the distribution with macroparticles (see Section 2.5). With a more analytical approach in mind, we turn to approximations of the VP system which sample the phase space in different ways.

2.2 Perturbation Theory

The standard analytical approach is to take momentum moments of the Vlasov equation as a proxy for the full VP system. The moment equations can then be solved perturbatively. We now define the first few moments of the Vlasov distribution f. Recall that the zeroth order moment was defined in Eq. (2.10). The first and second moments are defined as follows (see, e.g., [36])

$$\rho(\mathbf{x}, t) \mathbf{v}(\mathbf{x}, t) =: \int \mathrm{d}^3 \mathbf{p} \, \frac{\mathbf{p}}{ma} \, f(\mathbf{x}, \mathbf{p}, t) , \qquad (2.13)$$

$$\rho(\mathbf{x}, t) \mathbf{v}_i(\mathbf{x}, t) \mathbf{v}_j(\mathbf{x}, t) + \sigma_{ij}(\mathbf{x}, t) =: \int \mathrm{d}^3 \mathbf{p} \, \frac{p_i p_j}{(ma)^2} \, f(\mathbf{x}, \mathbf{p}, t) , \qquad (2.14)$$

where σ_{ij} is the velocity dispersion tensor, describing deviations from single-stream flow. Taking the zeroth moment of the Vlasov equation (Eq. 2.12), we get the continuity equation (we drop the $\mathbf{x}, \mathbf{p}, t$ dependence for convenience)

$$\frac{\partial \rho}{\partial t} + \frac{1}{a} \nabla \cdot (\rho \mathbf{v}) = 0 . \qquad (2.15)$$

The first moment gives the Euler equation

$$\frac{\mathrm{d}(\rho \mathbf{v})}{\mathrm{d}t} + H\rho \mathbf{v} + \frac{1}{a}(\rho \nabla \phi) + \frac{1}{a} \nabla \cdot \left(\rho \mathbf{v} \otimes \mathbf{v} + \sigma_{ij} \right) = 0 , \qquad (2.16)$$

and so on[2]. This leads to an infinite coupled hierarchy of equations, solving which is equivalent to solving the Vlasov equations directly. The velocity dispersion σ_{ij} is related to higher order moment equations, and a non-zero σ_{ij} generates higher moments of f which makes the truncation of the

---

[2] We keep the proper time t as the time variable, like in [37], and unlike [36] who use conformal time instead.

hierarchy impossible. Therefore, the only consistent truncation is at second order, by setting $\sigma_{ij} = 0$. We have arrived again at the single-stream approximation, or the dust model. This is equivalent to the following form of the distribution

$$f_{\mathrm{d}}(\mathbf{x}, \mathbf{p}) = \rho_{\mathrm{d}}(\mathbf{x})\delta^D \left[\mathbf{p} - \nabla\phi_{\mathrm{d}}(\mathbf{x})\right] , \tag{2.17}$$

where the subscript 'd' denotes dust, and δ^D is the three-dimensional Dirac delta. The model breaks down with shell crossing, accompanied by the formation of 'caustics' on small scales. Nevertheless, the dust model is an exact solution of the Vlasov equation, describing DM as a pressureless perfect fluid and works well in the linear regime of structure formation.

The methods to solve the system of Eq. (2.9, 2.15, 2.16) can be classified based on their preferred frames of reference. They are best understood in the context of fluid dynamics (see, e.g., [38]). An Eulerian frame of reference is characterised by a fixed mesh, providing a picture of the spatial distribution of the fluid velocity at each instant of time. The positions of individual fluid elements are time-dependent. The comoving coordinates $\mathbf{x}$ specify an Eulerian frame. In contrast, a Lagrangian frame follows specific fluid elements such that their Lagrangian coordinates are unchanged in time. This approach proves insightful when keeping track of individual particles or fluid elements. We now formalise perturbative solutions in the two pictures.

2.2.1 Standard (Eulerian) Perturbation Theory (SPT)

We begin by writing Eq. (2.15) in terms of the overdensity field using Eq. (2.6)

$$\frac{\partial\delta}{\partial t} + \frac{1}{a}\nabla \cdot \left[(1 + \delta)\mathbf{v}\right] = 0 . \tag{2.18}$$

Next, we make the assumption that the velocity field is completely described by its divergence $\theta(\mathbf{x}, t) := \nabla \cdot \mathbf{v}(\mathbf{x}, t)$. In other words, we assume that the vorticity $\mathbf{w}(\mathbf{x}, t) := \nabla \times \mathbf{v}(\mathbf{x}, t) = 0$. Under the assumption $\sigma_{ij} = 0$, if the initial vorticity vanishes, there is no vorticity at later times [36]. Even if the primordial vorticity is nonzero, it decays due to expansion in the linear regime. Thus, we are justified in making the assumption that $\mathbf{w} = 0$. We can thus make the Euler equation scalar by taking its divergence, and set $\sigma_{ij} = 0$. This gives

$$\frac{\partial\theta}{\partial t} + H\theta + 4\pi G\bar{\rho}a\delta = -\frac{1}{a}\nabla \cdot (\mathbf{v} \cdot \nabla\mathbf{v}) , \tag{2.19}$$

where we have used the Poisson equation to introduce δ. The assumption of perturbation theory (PT) is that Eq. (2.18, 2.19) can be solved by expanding the fields (δ, θ) about their linear solutions

$$\delta(\mathbf{x}, t) = \sum_{n=1}^{\infty} \delta^{(n)}(\mathbf{x}, t) , \qquad \theta(\mathbf{x}, t) = \sum_{n=1}^{\infty} \theta^{(n)}(\mathbf{x}, t) , \tag{2.20}$$

where $\delta^{(\mathrm{n})}, \theta^{(n)}$ are proportional to the nth power of the initial overdensity field. In effect, this means that we start with the linear order solution by dropping all terms of order two or higher in δ, θ in Eq. (2.18, 2.19), linearising about this solution, and then again dropping all higher order terms, and so on to the desired order [39].

The linearised continuity equation is

$$\frac{\partial \delta^{(1)}}{\partial t} + \frac{1}{a}\theta^{(1)} = 0 \ , \tag{2.21}$$

and the linearised Euler equation is

$$\frac{\partial \theta^{(1)}}{\partial t} + H\theta^{(1)} + 4\pi G\bar{\rho}a\delta = 0 \ . \tag{2.22}$$

We can take the time derivative of Eq. (2.21) and use Eq. (2.22) to eliminate θ. This gives

$$\frac{\partial^2 \delta^{(1)}}{\partial t^2} + 2H\frac{\partial \delta^{(1)}}{\partial t} - 4\pi G\bar{\rho}\delta^{(1)} = 0 \ . \tag{2.23}$$

Following the argument in [40], we see that while $\delta = \delta(\mathbf{x}, t)$, $\mathbf{x}$ does not appear explicitly in Eq. (2.23). We can treat this like a linear, homogeneous, ordinary differential equation. It is second order, and has two solutions which can be factorised. The general solution can thus be written as

$$\delta^{(1)}(\mathbf{x}, t) = D_+(t)A(\mathbf{x}) + D_-(t)B(\mathbf{x}) \ , \tag{2.24}$$

where $D_\pm(t)$ are the time-dependent growth factors, and $A(\mathbf{x})$ and $B(\mathbf{x})$ are arbitrary position-dependent functions. Then, using Eq. (2.21), we can obtain

$$\theta^{(1)}(\mathbf{x}, t) = -a(t)\left[\frac{\mathrm{d}D_+(t)}{\mathrm{d}t}A(\mathbf{x}) + \frac{\mathrm{d}D_-(t)}{\mathrm{d}t}B(\mathbf{x})\right] \ . \tag{2.25}$$

In the EdS universe,

$$\begin{aligned} D_+(t) &= a(t) \ , \\ D_-(t) &= a^{-3/2}(t) \ . \end{aligned} \tag{2.26}$$

Notice that D_+ is an increasing function of time, and D_- is a decreasing function of time. Therefore, D_- would decay away quickly even if it was nonzero at an earlier time. Only D_+ is responsible for the growth of gravitational instabilities [31, 40]. Thus, in linear theory, the EdS overdensity can be simply written as

$$\delta^{(1)}(\mathbf{x}, t) = a(t)\delta_0(\mathbf{x}) \ , \tag{2.27}$$

and the velocity field as

$$\theta^{(1)}(\mathbf{x}, t) = -a^2(t)\dot{a}(t)\delta_0(\mathbf{x}) \ , \tag{2.28}$$

where $\delta_0(\mathbf{x})$ is the initial overdensity.

To make the transition to nonlinear theory, it is common practice to work in Fourier space, where the nonlinearities are interpreted as the coupling of Fourier modes which were assumed independent in linear theory. The Fourier convention for an arbitrary function $h(\mathbf{x}, t)$ is as follows

$$\begin{aligned} \widetilde{h}(\mathbf{k}, t) &= \frac{1}{(2\pi)^3}\int \mathrm{d}^3\mathbf{x} \ h(\mathbf{x}, t)e^{-i\mathbf{k}\cdot\mathbf{x}} \ , \\ h(\mathbf{x}, t) &= \int \mathrm{d}^3\mathbf{k} \ \widetilde{h}(\mathbf{k}, t)e^{i\mathbf{k}\cdot\mathbf{x}} \ . \end{aligned} \tag{2.29}$$

We can move Eq. (2.18, 2.19) to Fourier space to get

$$a\frac{\partial \widetilde{\delta}(\mathbf{k}, t)}{\partial t} + \widetilde{\theta}(\mathbf{k}, t) = -\int d^3\mathbf{k}_1 \, d^3\mathbf{k}_2 \, \delta^D(\mathbf{k} - \mathbf{k}_{12}) \, \alpha(\mathbf{k}_1, \mathbf{k}_2) \, \widetilde{\theta}(\mathbf{k}_1, t) \, \widetilde{\delta}(\mathbf{k}_2, t) \,, \tag{2.30}$$

$$a\frac{\partial \widetilde{\theta}(\mathbf{k}, t)}{\partial t} + \dot{a}(t)\widetilde{\theta}(\mathbf{k}, t) + 4\pi G\bar{\rho}a^2\widetilde{\delta} = -\int d^3\mathbf{k}_1 \, d^3\mathbf{k}_2 \, \delta^D(\mathbf{k} - \mathbf{k}_{12}) \, \beta(\mathbf{k}_1, \mathbf{k}_2) \, \widetilde{\theta}(\mathbf{k}_1, t) \, \widetilde{\delta}(\mathbf{k}_2, t) \,, \tag{2.31}$$

where

$$\alpha(\mathbf{k}_1, \mathbf{k}_2) := \frac{\mathbf{k}_{12} \cdot \mathbf{k}_1}{\mathbf{k}_1} \,, \qquad \beta(\mathbf{k}_1, \mathbf{k}_2) := \frac{k_{12}^2(\mathbf{k}_1 \cdot \mathbf{k}_2)}{2k_1^2 k_2^2} \,, \tag{2.32}$$

capture the nonlinearity of the equations via the coupling of Fourier modes $\mathbf{k}_1$ and $\mathbf{k}_2$. The perturbative solutions in EdS cosmology can be found in [36, 37, 39], and in general cosmologies in [36]. The proposed EdS solution is

$$\widetilde{\delta}(\mathbf{k}, t) = \sum_{n=1}^{\infty} a^n(t)\delta_n(\mathbf{x}) \,, \qquad \widetilde{\theta}(\mathbf{k}, t) = -\dot{a}(t)\sum_{n=1}^{\infty} a^n(t)\theta_n(\mathbf{k}) \,. \tag{2.33}$$

The nth order fields $\delta_n(\mathbf{k})$ and $\theta_n(\mathbf{k})$ can then be specified in terms of the linear fields $\delta_1(\mathbf{k})$ and $\theta_1(\mathbf{k})$ as

$$\widetilde{\delta}_n(\mathbf{k}) = \int d^3\mathbf{g}_1 \ldots \int d^3\mathbf{g}_n \, \delta^D(\mathbf{k} - \mathbf{g}_{1\ldots n}) \, F_n(\mathbf{g}_1 \ldots, \mathbf{g}_n) \, \widetilde{\delta}_1(\mathbf{g}_1) \ldots \widetilde{\delta}_1(\mathbf{g}_n) \,, \tag{2.34}$$

$$\widetilde{\theta}_n(\mathbf{k}) = \int d^3\mathbf{g}_1 \ldots \int d^3\mathbf{g}_n \, \delta^D(\mathbf{k} - \mathbf{g}_{1\ldots n}) \, G_n(\mathbf{g}_1 \ldots, \mathbf{g}_n) \, \widetilde{\delta}_1(\mathbf{g}_1) \ldots \widetilde{\delta}_1(\mathbf{g}_n) \,, \tag{2.35}$$

where $\mathbf{g}_{1\ldots n} = \mathbf{g}_1 + \ldots + \mathbf{g}_n$, and F_n, G_n are kernels obeying recurrence relations. The first order kernels $F_1 = G_1 = 1$, and for $n \geq 2$

$$F_n(\mathbf{g}_1, \ldots, \mathbf{g}_n) := \sum_{m=1}^{n-1} \frac{G_m(\mathbf{g}_1, \ldots, \mathbf{g}_m)}{(2n+3)(n-1)} \left[(2n+1)\alpha(\mathbf{k}_1, \mathbf{k}_2)F_{n-m}(\mathbf{g}_{m+1}, \ldots, \mathbf{g}_n) \right.$$
$$\left. + 2\beta(\mathbf{k}_1, \mathbf{k}_2)G_{n-m}(\mathbf{g}_{m+1}, \ldots, \mathbf{g}_n) \right] \,, \tag{2.36}$$

$$G_n(\mathbf{g}_1, \ldots, \mathbf{g}_n) := \sum_{m=1}^{n-1} \frac{G_m(\mathbf{g}_1, \ldots, \mathbf{g}_m)}{(2n+3)(n-1)} \left[3\alpha(\mathbf{k}_1, \mathbf{k}_2)F_{n-m}(\mathbf{g}_{m+1}, \ldots, \mathbf{g}_n) \right.$$
$$\left. + 2n\beta(\mathbf{k}_1, \mathbf{k}_2)G_{n-m}(\mathbf{g}_{m+1}, \ldots, \mathbf{g}_n) \right] \,, \tag{2.37}$$

where $\mathbf{k}_1 := \mathbf{g}_1 + \ldots + \mathbf{g}_m$, $\mathbf{k}_2 := \mathbf{g}_{m+1} + \ldots + \mathbf{g}_n$, and $\mathbf{k} := \mathbf{k}_1 + \mathbf{k}_2$. For example, the $n = 2$ kernels are

$$F_2(\mathbf{g}_1, \mathbf{g}_2) = \frac{5}{7} + \frac{1}{2}\frac{\mathbf{g}_1 \cdot \mathbf{g}_2}{g_1 g_2}\left(\frac{g_1}{g_2} + \frac{g_2}{g_1}\right) + \frac{2}{7}\frac{(\mathbf{g}_1 \cdot \mathbf{g}_2)^2}{g_1^2 g_2^2} \,, \tag{2.38}$$

$$G_2(\mathbf{g}_1, \mathbf{g}_2) = \frac{3}{7} + \frac{1}{2}\frac{\mathbf{g}_1 \cdot \mathbf{g}_2}{g_1 g_2}\left(\frac{g_1}{g_2} + \frac{g_2}{g_1}\right) + \frac{4}{7}\frac{(\mathbf{g}_1 \cdot \mathbf{g}_2)^2}{g_1^2 g_2^2} \,. \tag{2.39}$$

The kernels are often made symmetric in the Fourier modes by summing over all their permutations. In the 1D case, $F_n = G_n$, and [33] suggest an alternative formulation for the symmetric kernels

$$F_n^{(s)}(\{g_i\}) = G_n^{(s)}(\{g_i\}) = \frac{1}{n!} \frac{g^n}{\prod_{i=1}^n g_i} , \qquad (2.40)$$

where $g = g_1 + \ldots + g_n$. The equality of the kernels means that the two fields δ and θ are identical in 1D. We now demonstrate the calculation of $\delta(\mathbf{x})$, from which the velocity field is easily calculated. We can write the 1D version of Eq. (2.34), and take its inverse Fourier transform to obtain

$$\delta_n(x) = \int_{-\infty}^{\infty} dk \left[\int dg_1 \ldots \int dg_n \, \delta^D(k - g_{1\ldots n}) \, F_n(g_1, \ldots, g_n) \, \widetilde{\delta}_1(g_1) \ldots \widetilde{\delta}_1(g_n) \right] e^{ixk} . \quad (2.41)$$

Using the sifting property of the Dirac delta we obtain,

$$\int_{-\infty}^{\infty} dk \, \delta^D(k - g_{1\ldots n}) \, e^{ixk} = e^{ixg_{1\ldots n}} . \qquad (2.42)$$

Using this in Eq. (2.41),

$$\delta_n(x) = \int dg_1 \ldots \int dg_n \, e^{ixg_{1\ldots n}} \, F_n(g_1, \ldots, g_n) \, \widetilde{\delta}_1(g_1) \ldots \widetilde{\delta}_1(g_n) . \qquad (2.43)$$

Using eq. (2.43), the overdensity can be computed to any order. For the trivial case $n = 1$, $F_1 = 1$, and we simply obtain the linear overdensity. For $n = 2$,

$$F_2^{(s)}(g_1, g_2) = 1 + \frac{1}{2}\left(\frac{g_1}{g_2} + \frac{g_2}{g_1}\right) , \qquad (2.44)$$

$$
\begin{aligned}
\delta_2(x) &= \int dg_1 \int dg_2 \, e^{ix(g_1+g_2)} \left[1 + \frac{1}{2}\left(\frac{g_1}{g_2} + \frac{g_2}{g_1}\right)\right] \widetilde{\delta}_1(g_1)\widetilde{\delta}_1(g_2) \\
&= \int dg_1 \int dg_2 \, e^{ix(g_1+g_2)} \, \widetilde{\delta}_1(g_1)\widetilde{\delta}_1(g_2) \\
&\quad + \frac{1}{2} \int dg_1 \int dg_2 \, e^{ix(g_1+g_2)} \left(\frac{g_1}{g_2}\right) \widetilde{\delta}_1(g_1)\widetilde{\delta}_1(g_2) \\
&\quad + \frac{1}{2} \int dg_1 \int dg_2 \, e^{ix(g_1+g_2)} \left(\frac{g_2}{g_1}\right) \widetilde{\delta}_1(g_1)\widetilde{\delta}_1(g_2) \\
&= \int dg_1 \, e^{ixg_1} \, \widetilde{\delta}_1(g_1) \int dg_2 \, e^{ixg_2} \, \widetilde{\delta}_1(g_2) \\
&\quad + \frac{1}{2} \int dg_1 \, e^{ixg_1} \, ig_1 \widetilde{\delta}_1(g_1) \int dg_2 \, e^{ixg_2} \left(\frac{\widetilde{\delta}_1(g_2)}{ig_2}\right) \\
&\quad + \frac{1}{2} \int dg_1 \, e^{ixg_1} \left(\frac{\widetilde{\delta}_1(g_1)}{ig_1}\right) \int dg_2 \, e^{ixg_2} \, ig_2 \widetilde{\delta}_1(g_2) \\
&= \delta_1^2(x) + \frac{d\delta_1(x)}{dx} \int_x^{\infty} dx' \, \delta_1(x') ,
\end{aligned}
\qquad (2.45)
$$

15

where the last step follows from properties of the Fourier transform. The SPT solution up to second order can thus be written in terms of only δ_1 as

$$\delta(x,t) = a(t)\delta_1(x) + a^2(t)\left(\delta_1^2(x) + \frac{\mathrm{d}\delta_1(x)}{\mathrm{d}x}\int_x^\infty \mathrm{d}x'\,\delta_1(x')\right)\,,\tag{2.46}$$

which can be written in terms of the initial overdensity using Eq. (2.27). Even in the simplified universe which is the focus of this work, higher-order solutions are difficult to compute by hand. For the SPT results in Chapter 4, we use the computer algebra module SymPy [41] to compute the kernels using Eq. (2.40), and follow the procedure illustrated in Eq. (2.45).

2.2.2 Lagrangian Perturbation Theory (LPT)

As we will show in Chapter 4, SPT fails to accurately describe the overdensity and velocity fields beyond the linear regime. Fortunately, the Lagrangian picture fares better in the mildly nonlinear regime. Specifically, linear order LPT (1LPT) – called the Zeldovich approximation [42] – is an exact solution in 1D until shell crossing. The Zeldovich approximation follows the particle trajectories through the displacement field $\mathbf{s}(\mathbf{q})$ which maps the Eulerian coordinates $\mathbf{x}$ to their initial (Lagrangian) coordinates $\mathbf{q}$ as

$$\mathbf{x}(\mathbf{q},t) = \mathbf{q} + \mathbf{s}(\mathbf{q},t)\,,\tag{2.47}$$

with

$$\mathbf{s}(\mathbf{q},t) = D_+(t)\mathbf{u}(\mathbf{q})\,,\tag{2.48}$$

where $\mathbf{u}(\mathbf{q})$ is the initial velocity field. The velocity at any time t can be obtained by differentiating Eq. (2.47) with respect to time

$$\mathbf{v}(\mathbf{q},t) = \dot{a}(t)\mathbf{u}(\mathbf{q})\,.\tag{2.49}$$

Since the initial velocity is assumed to be irrotational (vanishing vorticity), it can be described as the gradient of a scalar velocity potential Φ_0

$$\mathbf{u}(\mathbf{q}) = -\nabla\Phi_0(\mathbf{q})\,.\tag{2.50}$$

The velocity potential is related to the Newtonian gravitational potential ϕ as

$$\Phi_0 = \frac{2}{3H^2 a^3}\phi\,.\tag{2.51}$$

The density evolution follows from the conservation of mass. We assume that the mass of a fluid element in an Eulerian frame is the same as its mass in a Lagrangian frame [31]

$$\mathrm{d}M = \bar{\rho}\mathrm{d}^3\mathbf{q} = \rho(\mathbf{x},t)\mathrm{d}^3\mathbf{x}\,,\tag{2.52}$$

$$\frac{\rho(\mathbf{x},t)}{\bar{\rho}} = \frac{\mathrm{d}V_e}{\mathrm{d}V_l} = J(\mathbf{q},t)\,,\tag{2.53}$$

where $\mathrm{d}V_e = \mathrm{d}^3\mathbf{x}$ and $\mathrm{d}V_l = \mathrm{d}^3\mathbf{q}$ are the Eulerian and Lagrangian volume elements, and $J(\mathbf{q},t)$ is the

Jacobian of the transformation given by Eq. (2.47)

$$J(\mathbf{q}, t) = \left| \delta_{ij} - D_+(t) \frac{\partial^2 \Phi_0}{\partial q_i \partial q_j} \right| \, . \tag{2.54}$$

Introducing the overdensity field, we get

$$1 + \delta(\mathbf{x}) = \frac{1}{J(\mathbf{q}, t)} \, . \tag{2.55}$$

If we define the following deformation tensor

$$d_{ij} := \frac{\partial^2 \Phi_0}{\partial q_i \partial q_j} \, , \tag{2.56}$$

we can write the Jacobian in terms of its eigenvalues $\lambda_1, \lambda_2, \lambda_3$ as

$$J(\mathbf{q}, t) = \left[1 - D_+(t)\lambda_1(\mathbf{q}) \right] \left[1 - D_+(t)\lambda_2(\mathbf{q}) \right] \left[1 - D_+(t)\lambda_3(\mathbf{q}) \right] \, . \tag{2.57}$$

It is clear from Eq. (2.47) and (2.57) that at some point $\mathbf{q}$ in Lagrangian space, the trajectories of two particles intersect, i.e., two particles which started out at distinct Lagrangian positions $\mathbf{q}_1$ and $\mathbf{q}_2$ occupy the same Eulerian position $\mathbf{x}$. This corresponds to the formation of a shell-crossing singularity

$$1 - D_+(t)\lambda_1(\mathbf{q}) = 0 \, . \tag{2.58}$$

At this singularity, the overdensity field becomes infinite, and a set of such points forms a caustic in Eulerian space. In 1D, at the instant of shell crossing there is one point of infinite density. At the next instant, the density at this point becomes finite, and two neighbouring points develop infinite density. Between these two points, there are in total three streams. Two of these streams form the boundary of the collapsing 'pancake', and they move away from each other, increasing the thickness of the pancake. In the region between these two streams, any small scale effects are washed out. The singularity at the instant of shell crossing, and the pair of singularities forming the boundary of the pancake at each instant after shell crossing are two distinct types of singularities (Fig. 2.1). A detailed discussion of singularities in the Zeldovich approximation for the 1D and 2D case can be found in [43].

In the 1D EdS universe, the overdensity can be written as

$$1 + \delta(x) = \left| 1 - a(t) \frac{\partial^2 \Phi_0}{\partial q^2} \right|^{-1}$$
$$= \left| 1 - a(t)\delta_0(q) \right|^{-1} \, . \tag{2.59}$$

Also, the velocity is given by

$$v(q, t) = H_0 a^{-1/2} u(q) \, . \tag{2.60}$$

since $\dot{a}(t) = H_0 a^{-1/2}$ in EdS cosmology.

It was shown in [33] that in 1D, the infinite order solutions in SPT and LPT are identical. Until shell crossing, 1D linear LPT is exact, and we will compare our other methods to it. However, after
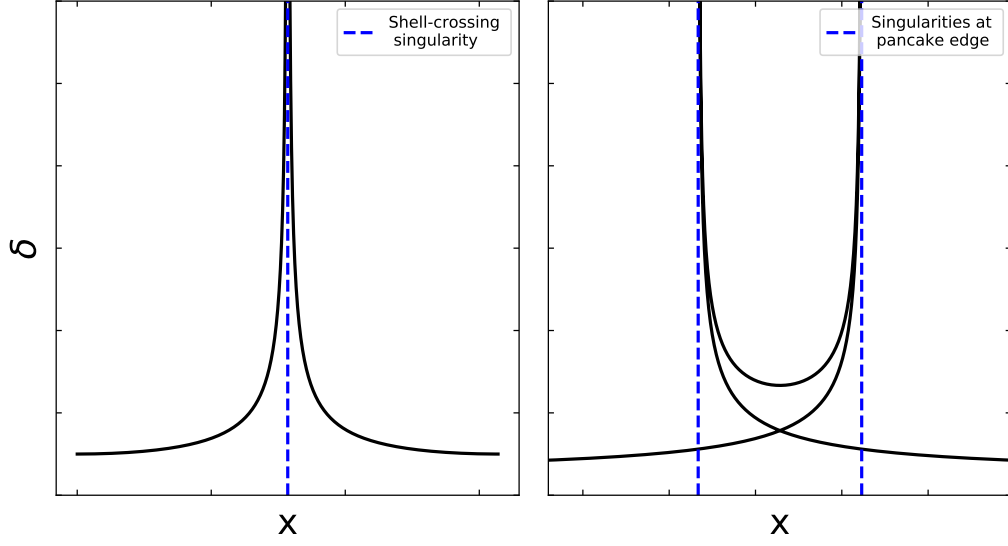
Figure 2.1: Singularities in the 1D Zeldovich approximation

shell crossing, the dust model breaks down, and we cannot use PT. There have been attempts to extend the applicability of the dust model beyond shell crossing. For example, [44] introduce the phenomenological 'adhesion approximation', where the dust model is extended by adding an artificial viscosity term to Eq. (2.19). In [45], the Newtonian potential ϕ is assumed to remain the same as in the linear regime so that the Poisson equation reads

$$\nabla^2 \phi(\mathbf{x}, t) = 4\pi G \bar{\rho} a^2 \delta_1(\mathbf{x}, t) \, , \tag{2.61}$$

where $\delta_1(\mathbf{x}, t) = D_+(t)\delta_1(\mathbf{x})$. This is called the 'linear potential approximation'. Along similar lines, the 'frozen-flow approximation' assumes that the velocity field remains the same as in the linear regime [46]. A detailed account of these approximations can be found in [31], and a direct comparison of these approximations to LPT can be found in [47]. For a more satisfying analytical description, however, we must turn away from the dust model.

2.3 The Schrödinger-Poisson System

A novel approach to model CDM was introduced in [48]. Here, the DM distribution is approximated by a complex scalar field $\psi(\mathbf{x}, t)$ obeying the coupled Schrödinger-Poisson (SP) equations

$$i\hbar \frac{\partial \psi}{\partial t} = -\frac{\hbar^2}{2ma^2} \nabla^2 \psi + m\phi\psi \, , \tag{2.62}$$

$$\nabla^2 \phi = 4\pi G \bar{\rho} a^2 \left(|\psi|^2 - 1 \right) \, , \tag{2.63}$$

where $\hbar$ is a free parameter controlling resolution in phase space.

The SP system can be interpreted as a nonrelativistic limit of the Klein-Gordon-Einstein equations,

in which case CDM behaves like a noninteracting nonrelativistic Bose Einsten condensate [49, 50]. Despite being a position dependent function, $\psi(\mathbf{x}, t)$ encodes both position and momentum space information. To extract the latter from ψ, one must construct a distribution function. [51] paints a detailed picture of the correspondence between classical distribution functions and quantum phase space descriptions. It was demonstrated in [48] that the Husimi distribution – a coarse-grained form of the more common Wigner distribution – provides a good description of classical phase space dynamics. [48, 52, 53] show that the SP system can follow phase space dynamics beyond shell crossing, and can provide an alternative to N-body simulations. [54–57] argue that SP is a genuine analytical tool to approximate VP. In this description, SP is a smoothed version of VP with $\hbar$ acting as the smoothing parameter. [58] show that the free-particle version of the SP equations (where the potential ϕ is set to zero) is analogous to the adhesion approximation, with a nonlinear 'quantum pressure' term acting as an artificial viscosity. [54] show that the method describes multistreaming as well as virialisation.

To make the position of SP in the space of all models more concrete, it is useful to start with a mapping to the dust model. This is known as the Madelung representation

$$\psi(\mathbf{x}) = \sqrt{\rho(\mathbf{x})} e^{i\Phi(\mathbf{x})/\hbar} \,, \tag{2.64}$$

where Φ is the peculiar velocity potential. Using Eq. (2.64) in Eq. (2.62) we get a dust-like system for ρ and Φ by separating the real and imaginary parts

$$\frac{\partial \rho}{\partial t} + \frac{1}{ma^2} \nabla \cdot (\rho \nabla \Phi) = 0 \,, \tag{2.65}$$

$$\frac{\partial \Phi}{\partial t} + \frac{1}{2ma^2} (\nabla \Phi)^2 + m\phi - \frac{\hbar^2}{2ma^2} \frac{\nabla^2 \sqrt{\rho}}{\sqrt{\rho}} = 0 \,. \tag{2.66}$$

This is identical to the fluid equations of the dust model with the exception of the term proportional to $\hbar^2$ – the quantum pressure term. This can be made even clearer with the substitution $\mathbf{v} = \nabla\Phi/m$, leading to

$$\frac{\partial \rho}{\partial t} + \frac{1}{a^2} \nabla \cdot (\rho \mathbf{v}) = 0 \,, \tag{2.67}$$

$$\frac{\partial \mathbf{v}}{\partial t} + \frac{1}{a^2} \mathbf{v} \cdot \nabla \mathbf{v} + \phi - \frac{\hbar^2}{2ma^2} \nabla \left(\frac{\nabla^2 \sqrt{\rho}}{\sqrt{\rho}} \right) = 0 \,. \tag{2.68}$$

Notice that if $\rho = 0$, the Madelung representation develops singularities, and the analogy between SP and the dust model breaks down. These singularities arise after shell crossing. Also, it was found that velocity dispersion and vorticity are both generated in N-body simulations after shell crossing (see [59]). If the latter arises in a system, the velocity field is no longer irrotational, and cannot be expressed in terms of a potential. The velocity potential in the phase of the Madelung representation thus becomes invalid, and the representation breaks down. Although one cannot make the transformation from SP to the dust model after shell crossing, SP itself is free from such singularities and can continue to provide a good description of the dynamics.

In constructing a distribution from ψ, the Wigner distribution [60] would be a natural choice, as it

is often used to that effect in quantum mechanics. It is given by

$$f_{\text{W}}(\mathbf{x}, \mathbf{p}) = \int \frac{\mathrm{d}^3 \mathbf{x}'}{(\pi\hbar)^3} e^{\frac{2i\mathbf{p}\cdot\mathbf{x}'}{\hbar}} \psi(\mathbf{x} - \mathbf{x}')\psi^*(\mathbf{x} + \mathbf{x}') \,, \tag{2.69}$$

where ψ^* is the complex conjugate of ψ. The Wigner function is a *quasiprobability* distribution because it can take negative values, and therefore is not a true probability distribution function. Except for a few simple cases like the free particle or the harmonic oscillator, it does not lead to a classical probability distribution [51]. However, we can construct a coarse-grained Wigner function by smoothing it with a Gaussian filter in both position and momentum space, and the resulting distribution has a much better correspondence with classical mechanics

$$\bar{f}_{\text{W}}(\mathbf{x}, \mathbf{p}) = \int \frac{\mathrm{d}^3 \mathbf{x}' \, \mathrm{d}^3 \mathbf{p}'}{(2\pi\sigma_x\sigma_p)^3} \exp\left\{ \frac{-(\mathbf{x} - \mathbf{x}')^2}{2\sigma_x^2} \right\} \exp\left\{ \frac{-(\mathbf{p} - \mathbf{p}')^2}{2\sigma_p^2} \right\} f_{\text{W}}(\mathbf{x}', \mathbf{p}')$$

$$= \exp\left(\frac{\sigma_x^2}{2} \Delta_x + \frac{\sigma_p^2}{2} \Delta_p \right) f_{\text{W}}(\mathbf{x}', \mathbf{p}') \,, \tag{2.70}$$

where σ_x and σ_p represent the smoothing scales in $\mathbf{x}$ and $\mathbf{p}$ space respectively. For the coarse-grained Wigner function to be nonnegative, the two scales are bound by

$$\sigma_x \sigma_p \geq \frac{\hbar}{2} \,. \tag{2.71}$$

For the specific choice $\sigma_x \sigma_p = \hbar/2$, the distribution is called the Husimi distribution [61]. It can be constructed directly from ψ as

$$f_{\text{H}}(\mathbf{x}, \mathbf{p}) = \left| \int \mathrm{d}^3 \mathbf{x}' K_{\text{H}}(\mathbf{x}, \mathbf{x}', \mathbf{p}) \psi(\mathbf{x}') \right|^2 \,, \tag{2.72}$$

where

$$K_{\text{H}}(\mathbf{x}, \mathbf{x}', \mathbf{p}) = \left(\frac{1}{2\pi\hbar} \right)^{3/2} \left(\frac{1}{2\pi\sigma_x^2} \right)^{3/4} \exp\left[-\frac{(\mathbf{x} - \mathbf{x}')^2}{4\sigma_x^2} - \frac{i}{\hbar} \mathbf{p} \cdot (\mathbf{x}' - \frac{\mathbf{x}}{2}) \right] \,. \tag{2.73}$$

It is insightful to look at the relevant scales involved. If we are interested in structures of size L, the SP system approximates VP if

$$\lambda_{\text{deB}} \ll \sigma_x \ll L \,, \tag{2.74}$$

where $\lambda_{\text{deB}} := \hbar/mv$ is the de Broglie wavelength. Therefore, to resolve structure on small-scales, one must be careful in the choice of $\hbar$. The SP-VP correspondence can be investigated by computing a Vlasov-like equation for f_{H} as in [62]

$$\frac{\partial f_{\text{H}}}{\partial t} + \frac{\mathrm{d}\mathbf{x}}{\mathrm{d}t} \cdot \frac{\partial f_{\text{H}}}{\partial \mathbf{x}} + \frac{\mathrm{d}\mathbf{p}}{\mathrm{d}t} \cdot \frac{\partial f_{\text{H}}}{\partial \mathbf{p}} + O(\hbar) + O(\hbar^2) + \ldots = 0 \,, \tag{2.75}$$

i.e., we should expect the two systems to be identical in the limit $\hbar \to 0$. For more details on this correspondence, see [56].

Besides offering a way to resolve dynamics beyond shell crossing, the SP system opens up the

possibility of direct calculation of higher order moments of the distribution, notably the velocity dispersion. In Chapter 4, we explicitly compute the velocity dispersion after solving the SP equations, and showcase the deviations of this quantity from the assumption of the dust model. It should be noted that the SP system is not limited to CDM, but can also be used to study warm initial conditions.

2.4 Hierarchy of moments and cumulants

Now, we sketch the prescription to calculate the moments and cumulants of the distribution function in 1D. Given a generic distribution function f, we can define the generating functional $G[J]$ as follows (see, e.g., [54, 63])

$$G[J] = \int \mathrm{d}p \, \exp(ipJ) f \ . \tag{2.76}$$

This functional allows us to generate the moments and cumulants from f. The moments are given by

$$M^{(n)} = (-i)^n \left. \frac{\partial^n G}{\partial J^n} \right|_{J=0} \ , \tag{2.77}$$

and the cumulants by

$$C^{(n)} = (-i)^n \left. \frac{\partial^n \ln G}{\partial J^n} \right|_{J=0} \ . \tag{2.78}$$

To see the this in action, let us consider the generating functional for the dust model (to simplify notation, we use the subscript ',i' to denote a partial derivative with respect to x, such that the number of is correspond to the order of the derivative)

$$G_\mathrm{d}[J] = \rho \exp\left(i\Phi_{,i}J\right) \ , \tag{2.79}$$

where ρ is the mass density, and the Φ is the peculiar velocity potential. We can now generate the moments and cumulants for the dust model. The moments are given by

$$
\begin{aligned}
M_\mathrm{d}^{(0)} &= G_\mathrm{d}\big|_{J=0} \\
&= \rho \ ,
\end{aligned} \tag{2.80a}
$$

$$
\begin{aligned}
M_\mathrm{d}^{(n \geq 1)} &= (-i)^n \left. \frac{\partial^n G_\mathrm{d}}{\partial J^n} \right|_{J=0} \\
&= \rho \Phi_{,i}^n \ ,
\end{aligned} \tag{2.80b}
$$

and the cumulants by

$$
\begin{aligned}
C_\mathrm{d}^{(0)} &= \ln G_\mathrm{d}\big|_{J=0} \\
&= \ln \rho \ ,
\end{aligned} \tag{2.81a}
$$

$$
\begin{aligned}
C_\mathrm{d}^{(1)} &= (-i) \left. \frac{\partial \ln G_\mathrm{d}}{\partial J} \right|_{J=0} \\
&= \Phi_{,i} \ ,
\end{aligned} \tag{2.81b}
$$

$$C_{\mathrm{d}}^{(n\geq 2)} = (-i)^2 \left. \frac{\partial^2 \ln G_{\mathrm{d}}}{\partial J^2} \right|_{J=0}$$

$$= 0 \ . \tag{2.81c}$$

We see formally that the dust model truncates the cumulant hierarchy such that cumulants of all orders higher than two are zero. The second order cumulant contains the velocity dispersion information that is absent in the dust model, but can be calculated for the SP system.

It turns out that the Wigner moments can be calculated directly from ψ without building the distribution. The generating functional for the Wigner distribution is given as ([63])

$$G_{\mathrm{W}}[J] = \psi\left(x + \frac{\hbar}{2}J\right)\psi^*\left(x - \frac{\hbar}{2}J\right) \ , \tag{2.82}$$

where ψ^* is the complex conjugate of ψ. Thus, the first three Wigner moments are

$$M_{\mathrm{W}}^{(0)} = \left. G_{\mathrm{W}} \right|_{J=0}$$

$$= \psi\psi^* \ , \tag{2.83a}$$

$$M_{\mathrm{W}}^{(1)} = (-i)\left. \frac{\partial G_{\mathrm{W}}}{\partial J} \right|_{J=0}$$

$$= -\frac{i\hbar}{2}\left(\psi_{,i}\psi^* - \psi\psi^*_{,i}\right) \ , \tag{2.83b}$$

$$M_{\mathrm{W}}^{(2)} = (-i)^2 \left. \frac{\partial^2 G_{\mathrm{W}}}{\partial J^2} \right|_{J=0}$$

$$= -\frac{\hbar^2}{4}\left(\psi_{,ii}\,\psi^* - 2\psi_{,i}\psi^*_{,i} + \psi\psi^*_{,ii}\right) \ . \tag{2.83c}$$

All Wigner cumulants can be expressed in terms of the moments. The zeroth cumulant is

$$C_{\mathrm{W}}^{(0)} = \left. \ln G_{\mathrm{W}} \right|_{J=0}$$

$$= \ln M_{\mathrm{W}}^{(0)} \ , \tag{2.84}$$

the first cumulant is

$$C_{\mathrm{W}}^{(1)} = -i\left. \frac{\partial \ln G_{\mathrm{W}}}{\partial J} \right|_{J=0}$$

$$= -i\left. \frac{1}{G_{\mathrm{W}}}\frac{\partial G_{\mathrm{W}}}{\partial J} \right|_{J=0}$$

$$= \frac{M_{\mathrm{W}}^{(1)}}{M_{\mathrm{W}}^{(0)}} \ , \tag{2.85}$$

and the second cumulant is

$$
\begin{aligned}
C_{\mathrm{W}}^{(2)} &= (-i)^2 \left. \frac{\partial^2 \ln G_{\mathrm{W}}}{\partial J^2} \right|_{J=0} \\
&= -\left. \frac{\partial}{\partial J} \left[\frac{1}{G_{\mathrm{W}}} \frac{\partial \ln G_{\mathrm{W}}}{\partial J} \right] \right|_{J=0} \\
&= -\left. \frac{1}{G_{\mathrm{W}}^2} \left[G_{\mathrm{W}} \frac{\partial^2 G_{\mathrm{W}}}{\partial J^2} - \left(\frac{\partial G_{\mathrm{W}}}{\partial J} \right) \left(\frac{\partial G_{\mathrm{W}}}{\partial J} \right) \right] \right|_{J=0} \\
&= \frac{M_{\mathrm{W}}^{(2)}}{M_{\mathrm{W}}^{(0)}} - \frac{\left[M_{\mathrm{W}}^{(1)} \right]^2}{\left[M_{\mathrm{W}}^{(0)} \right]^2} \ .
\end{aligned}
\tag{2.86}
$$

To transition from Wigner to Husimi, we can use Eq. (2.70). The Husimi generating functional is thus given as

$$
G_{\mathrm{H}}[J] = \exp\left(\frac{\sigma_x^2}{2} \Delta_x + \frac{\sigma_p^2}{2} J^2 \right) G_{\mathrm{W}}[J] \ .
\tag{2.87}
$$

The Husimi moments are therefore equal to spatially smoothed versions of their Wigner counterparts. If we indicate smoothing by a bar over the smoothed quantity, we can write the Husimi moments in terms of the Wigner moments as

$$
M_{\mathrm{H}}^{(n)} = \bar{M}_{\mathrm{W}}^{(n)} \ .
\tag{2.88}
$$

The cumulant relations obtained in Eq. (2.84-2.86) hold for the Husimi cumulants as well. Thus, we can express the first three Husimi cumulants in terms of the first three Wigner moments as follows

$$
C_{\mathrm{H}}^{(0)} = \ln \bar{M}_{\mathrm{W}}^{(0)} \ ,
\tag{2.89}
$$

$$
C_{\mathrm{H}}^{(1)} = \frac{\bar{M}_{\mathrm{W}}^{(1)}}{\bar{M}_{\mathrm{W}}^{(0)}} \ ,
\tag{2.90}
$$

$$
C_{\mathrm{H}}^{(2)} = \frac{\bar{M}_{\mathrm{W}}^{(2)}}{\bar{M}_{\mathrm{W}}^{(0)}} - \frac{\left[\bar{M}_{\mathrm{W}}^{(1)} \right]^2}{\left[\bar{M}_{\mathrm{W}}^{(0)} \right]^2} \ .
\tag{2.91}
$$

Here, it is important to note that moments of Husimi distribution hold the same content as those of the dust model as long as the Madelung representation is free of singularities, i.e. before shell crossing. After the first shell crossing, the system generates cumulants $C_{\mathrm{d}}^{(n \geq 2)}$ and the dust model breaks down. However, the SP system is unaffected by this, and we can continue to extract physically meaningful information from the higher moments. With regards to the overall picture, the Husimi distribution approximates the Vlasov distribution, and we can assign the same meaning to the Husimi moments as we did to the Vlasov moments. Returning to our definition of the moments in Eq. (2.10, 2.13, 2.14), we can see that

$$
M_{\mathrm{H}}^{(0)} = \rho \ ,
\tag{2.92}
$$

$$M_{\text{H}}^{(1)} = \rho v \ , \tag{2.93}$$

$$M_{\text{H}}^{(2)} = \rho v^2 + \sigma \ . \tag{2.94}$$

Thus we have an expression for the velocity dispersion σ in terms of the moments

$$\sigma = M_{\text{H}}^{(2)} - \frac{\left[M_{\text{H}}^{(1)} \right]^2}{M_{\text{H}}^{(0)}} \ . \tag{2.95}$$

This is a general relation for any distribution function that solves the Vlasov equation. For example, if we substitute M_{d} for M_{H}, we can see that the velocity dispersion is indeed zero in the dust model. The equation also offers a straightforward way to calculate the velocity dispersion. Since we can construct all moments from ψ without building the Husimi distribution, this is numerically efficient.

2.5 Numerical Simulations

Numerical (N-body) simulations sample the phase space by approximating the Vlasov distribution by macroparticles in two steps. Given an initial particle configuration, one first calculates the gravitational force which results from the configuration, and then computes the motion of the particles due to the force. The simulation follows individual particle trajectories, and the mass resolution is set by the number of particles N_{p}. The distribution takes the following form

$$f_{\text{N-body}}(\mathbf{x}, \mathbf{p}, t) = A \sum_{i=1}^{N_{\text{p}}} \delta^D \left[\mathbf{x} - \mathbf{x}_i(t) \right] \delta^D \left[\mathbf{p} - \mathbf{p}_i(t) \right] \ , \tag{2.96}$$

where A is some appropriate normalisation. At each time-step, N-body methods solve the Poisson equation to determine the force, and then use Newton's equation of motion to move the particles according to the calculated force. The relevant equations are (see, e.g., [64])

$$\frac{\mathrm{d}^2 \mathbf{x}}{\mathrm{d}t^2} + 2H \frac{\mathrm{d}\mathbf{x}}{\mathrm{d}t} = -\frac{\nabla \phi}{a^2} \ , \tag{2.97}$$

$$\nabla^2 \phi = \frac{3H_0^2 \Omega_0}{2a} \delta \ , \tag{2.98}$$

where the Poisson equation is modified from Eq. (2.9) using Eq. (1.23). We can simplify this by changing the time variable

$$\mathrm{d}\tau = H_0 \frac{\mathrm{d}t}{a^2} \ . \tag{2.99}$$

The modified equations then read

$$\frac{\mathrm{d}^2 \mathbf{x}}{\mathrm{d}\tau^2} = -\frac{3}{2} \Omega_0 a^2 \nabla \chi \ , \tag{2.100}$$

$$\nabla^2 \chi = \frac{\delta}{a} \ . \tag{2.101}$$

Updating the particle positions and velocities at each time-step is usually accomplished using time integrators (e.g. the Leapfrog integrator). This is a computation of order $O(N_{\rm p})$. The different N-body codes differ mainly in the way they solve the Poisson equation and compute the forces. They can be broadly classified as follows

- **Direct Summation**: This is a method of order $O(N_{\rm p}^2)$ in which the force on a particle is calculated by directly summing the forces due to all other particles. For this reason, it is also called the Particle-Particle (PP) method.

- **Tree Algorithm**: In this method, the force on a particle from a distant region is approximated by the force from the centre of mass of that region. In this manner, the particle distribution is decomposed into a hierarchical tree [1]. The method is of order $O(N_{\rm p} \log N_{\rm p})$.

- **Particle-Mesh (PM) Method**: In this method, the force is computed on a fixed grid of size $N_{\rm g}$, usually by solving the Poisson equation in Fourier space. It is of order $O(N_{\rm p}, N_{\rm g}^3 \log N_{\rm g})$, where $N_{\rm g}$ is the number of grid points [64, 65].

- **Hybrid Methods**: A PP+PM (P^3M) method uses direct summation for the calculation of force from nearby particles, and uses a fixed grid in the rest of the box [65]. Along similar lines, the tree algorithm can be used for short-range calculations, while using a fixed grid elsewhere. The grid used in PM methods can be refined into rectangular subgrids, resulting in adaptive mesh refinement (AMR) codes [66]. If the subgrids are not rectangular, but instead have a tree structure, the resulting method is called the adaptive refinement tree (ART) method [67].

Apart from force computation and particle motion, there are a few physical considerations that an N-body code must take into account [64]. Firstly, the simulation box cannot be as large as the observable universe, and at the same time also resolve structures on galactic scales. This necessitates the use of periodic boundary conditions. Further, the box size has to be large enough so that the perturbations averaged over that scale must be small. Finally, the particle number must be large enough to allow sufficient mass resolution on scales of interest, and these particles must interact in a collisionless manner.

As we develop the analytical methods that describe nonlinear clustering, N-body codes are the standard tools to compare our results to. For a review of N-body codes see [68].

Numerical Methods

For the numerical implementation of all our methods, we define a 1D box of size L with a discrete grid containing N grid points. The grid points are then defined as

$$x_j = j\Delta x \,, \quad \Delta x = \frac{L}{N} \,, \tag{3.1}$$

where $j \in \{0, 1, \dots, N-1\}$. The grid is defined to be periodic, such that the points x_0 and x_N are mapped onto each other.
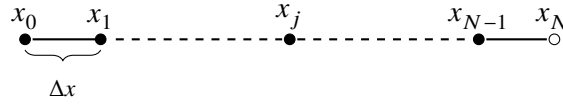

Figure 3.1: Coordinate grid.

Now, consider the two functions

$$f(x) = \exp(ikx) \,, \qquad g(x) = \exp(ik'x) \,, \tag{3.2}$$

where k denotes the Fourier modes (wavevectors) corresponding to x. In general, $f(x) \neq g(x)$ if $k \neq k'$. However, for functions on a discrete grid

$$f_j = \exp(ikx_j) \,, \qquad g_j = \exp(ik'x_j) \,, \tag{3.3}$$

$$f_j = g_j \ \forall j \,, \quad \text{if } k - k' = \frac{2\pi n}{\Delta x} \ \text{for } n \in \mathbb{Z} \,. \tag{3.4}$$

In other words, for all complex exponentials e^{ikx}, there exist infinitely many complex exponentials $e^{ik'x}$ (aliases) such that the two are identical on the discrete grid even though $k \neq k'$. This is known as aliasing. In order to avoid this, we must construct a Fourier grid as a bounded interval with length $2\pi/\Delta x$. The natural symmetric choice is the interval $[-\pi/\Delta x, \pi/\Delta x)$. With a choice of $L = 2\pi$, the grid can be written as

$$x \in [0, 2\pi) \,, \qquad k_x \in \left[-\frac{N}{2}, \frac{N}{2}\right) \,. \tag{3.5}$$

We can use a Fourier transform to move a function from real space to its corresponding Fourier space. This is useful when some operators are easier to apply in Fourier space than in real space. For example, a real space derivative (integral) is equivalent to multiplication (division) by the wavevector $i2\pi k/L$ in Fourier space.

3.1 Poisson Solver

In its general form, the Poisson equation can be written on our discrete 1D grid as follows

$$\frac{\partial^2 u}{\partial x_j^2} = g(x_j) , \qquad 0 \le x_j < L , \tag{3.6}$$

with the periodic boundary condition

$$u(x_0) = u(x_N) . \tag{3.7}$$

There are many ways to integrate the Poisson equation numerically. For example, simple finite difference (FD) schemes replace derivatives with linear difference operators. The resulting matrix equation can be solved, e.g., by Gaussian elimination. For integrating over more complicated volumes, the finite element method (FEM) can be used. In FEM, the first step is to multiply the (continuum) Poisson equation by a test function and then integrating to obtain a 'weak form' of the equation. Next, the domain is subdivided into smaller regions called 'elements', where the weak form is discretised. Finally, the solution $u(x_j)$ is approximated on this discretised domain using an appropriate basis function.

We solve the discrete Poisson equation directly in Fourier space, where the Laplacian operator becomes a product by $(i2\pi k/L)^2$. The algorithm for this solution can be written as

$$u(x_j) = \mathcal{F}^{-1} \left\{ \frac{\mathcal{F}[g(x_j)]}{(i2\pi k/L)^2} \right\} , \tag{3.8}$$

where the function value corresponding to $k = 0$ depends on the boundary conditions. The discrete Fourier transform operator $(\mathcal{F})$ is in general of order $O(N^2)$. However, the Fourier modes are symmetric about 0, and this fact can be exploited to reduce the computation involved. The most common such algorithm is the Fast Fourier Transform (FFT), first introduced in [69]. The FFT is of order $O(N \log N)$. For a detailed account of the various Poisson solvers, see [70].

3.2 Vlasov Solver

Numerical methods to solve the VP system may be broadly classified as

- **N-body Simulations**: As introduced in Section 2.5, these methods approximate the Vlasov distribution using macroparticles. N-body codes are the only well-developed technique to simulate dynamics in the nonlinear regime after the dust model becomes invalid.

- **Semi-Lagrangian Methods**: These methods exploit the Hamiltonian nature of the flow in phase space. They compute the distribution function by following the characteristic curves along which

the distribution remains constant [71]. This method suffers from an issue called 'filamentation' where the phase-space grid eventually becomes too coarse to resolve nonlinearities.

- **Eulerian Methods**: These include general finite difference schemes, or more specialised methods, e.g. the flux-corrected transport (FCT) approach of [72]. FCT considers the flux entering and leaving each volume element, and uses the conservation of flux to estimate the distribution function.

We use the semi-Lagrangian splitting method from [71] to solve the VP system. In 1D, the equations take the following form

$$\frac{\partial f}{\partial t} + \frac{p}{ma^2}\frac{\partial f}{\partial x} - m\frac{\partial \phi}{\partial x}\frac{\partial f}{\partial p} = 0 \; , \tag{3.9}$$

$$\frac{\partial^2 \phi}{\partial x^2} = \frac{3H_0^2}{2a}\left(\int dp\; f - 1\right) \; . \tag{3.10}$$

The key idea is to split the Vlasov equation in two parts at each time-step, and solve the new equations at successive half time-steps

$$\frac{\partial f}{\partial t} + \frac{p}{ma^2}\frac{\partial f}{\partial x} = 0 \; , \tag{3.11a}$$

$$\frac{\partial f}{\partial t} - m\frac{\partial \phi}{\partial x}\frac{\partial f}{\partial p} = 0 \; . \tag{3.11b}$$

These equations are a first order approximation of Eq. (3.9). Now, consider the differential of f

$$\mathrm{d}f = \frac{\partial f}{\partial t}\,\mathrm{d}t + \frac{\partial f}{\partial x}\,\mathrm{d}x + \frac{\partial f}{\partial p}\,\mathrm{d}p \; . \tag{3.12}$$

At each half time-step Δt, we make the assumption that first p and then x is held constant, while the other variable is allowed to change. This leads to the following splitting of Eq. (3.12)

$$\mathrm{d}f = \frac{\partial f}{\partial t}\,\mathrm{d}t + \frac{\partial f}{\partial x}\,\mathrm{d}x \; , \tag{3.13a}$$

$$\mathrm{d}f = \frac{\partial f}{\partial t}\,\mathrm{d}t + \frac{\partial f}{\partial p}\,\mathrm{d}p \; . \tag{3.13b}$$

From Liouville's theorem, we know that there exist characteristic curves along which the differential vanishes. These are the particle trajectories given by (x', p'). We can use the $\mathrm{d}f = 0$ condition to compare Eq. (3.11) and Eq. (3.13). Doing this for a discrete grid results in

$$\Delta x = \frac{p}{ma^2}\Delta t \; , \tag{3.14a}$$

$$\Delta p = -m\frac{\partial \phi}{\partial x}\Delta t \; , \tag{3.14b}$$

where $\Delta x = x - x'$ and $\Delta p = p - p'$. Therefore, evolving the distribution forward in time amounts to successive shifts or translations in position and then momentum space. This can be summarised as

follows

$$f(x, p, t + \Delta t) = f\left(x - \frac{p}{ma^2}\Delta t, p, t\right) , \tag{3.15a}$$

$$f(x, p, t + \Delta t) = f\left(x, p + m\frac{\partial \phi}{\partial x}\Delta t, t\right) . \tag{3.15b}$$

Before we write down the algorithm to carry out these shifts, it is useful to change the time variable from t to a, and rewrite the equations in a slightly different form (note that for an EdS Universe, $\dot{a} = H_0 a^{-1/2}$)

$$\dot{a}\frac{\partial f}{\partial a} + \frac{p}{ma^2}\frac{\partial f}{\partial x} - m\frac{\partial \phi}{\partial x}\frac{\partial f}{\partial p} = 0 , \tag{3.16}$$

$$\frac{\partial f}{\partial a} + \left(\frac{p}{mH_0 a^{3/2}}\right)\frac{\partial f}{\partial x} - \frac{m\sqrt{a}}{H_0}\frac{\partial \phi}{\partial x}\frac{\partial f}{\partial p} = 0 , \tag{3.17}$$

$$\frac{\partial f}{\partial a} + \lambda(a)\frac{\partial f}{\partial x} - \frac{\partial \bar{\phi}}{\partial x}\frac{\partial f}{\partial p} = 0 . \tag{3.18}$$

The Poisson equation then becomes

$$\frac{\partial^2 \bar{\phi}}{\partial x^2} = \frac{3H_0 m}{2\sqrt{a}}\left(\int dp \, f - 1\right) , \tag{3.19}$$

where

$$\lambda(a) = \frac{p}{mH_0 a^{3/2}} , \qquad \bar{\phi} = \frac{m\sqrt{a}}{H_0}\phi . \tag{3.20}$$

Finally, the algorithm can be written in the following steps

$$f^*(x, p) = f^n\left(x - \lambda\frac{\Delta a}{2}, p\right) , \tag{3.21a}$$

$$f^{**}(x, p) = f^*\left(x, p + \frac{\partial \bar{\phi}}{\partial x}\Delta a\right) , \tag{3.21b}$$

$$f^{n+1}(x, p) = f^{**}\left(x - \lambda\frac{\Delta a}{2}, p\right) , \tag{3.21c}$$

where the indices n and $n + 1$ are shorthand for discrete times a_n and a_{n+1}, with $\Delta a = a_{n+1} - a_n$, and the starred indices refer to intermediate times which are not defined on the grid. The gravitational field $\bar{\phi}$ is obtained by solving the Poisson equation after the first spatial shift has been carried out. Each step is implemented as follows

$$f^*(x, p) = \mathcal{F}_x^{-1}\left\{\mathcal{F}_x\left[f^n(x, p)\right]\exp\left(-ik_x\lambda\frac{\Delta a}{2}\right)\right\} , \tag{3.22a}$$

$$f^{**}(x, p) = \mathcal{F}_p^{-1}\left\{\mathcal{F}_p\left[f^*(x, p)\right]\exp\left(ik_p\frac{\partial \bar{\phi}}{\partial x}\Delta a\right)\right\} , \tag{3.22b}$$

$$f^{n+1}(x, p) = \mathscr{F}_x^{-1} \left\{ \mathscr{F}_x \left[f^{**}(x, p) \right] \exp\left(-ik_x \lambda \frac{\Delta a}{2}\right) \right\} , \tag{3.22c}$$

where $\mathscr{F}_{x(p)}$ is again the Fourier transform operator in position (momentum) space and k_x, k_p are the respective Fourier modes. To implement this algorithm, we need to compute six transforms between real and Fourier space at every time-step, and though each transform is of order $O(N \log N)$, the overall computation is expensive, especially in higher dimensions. To remedy this, [73] suggest working in the Fourier-Fourier transformed space (which can be entered by taking successive Fourier transforms with respect to x and p). This reduces the number of FFTs at each time-step to two. They also implement a filtration technique to reduce filamentation. This involves smoothing the distribution after a fixed number of time-steps to filter out any filaments. The implementation of filtration is straightforward in the Fourier-Fourier transformed space. However, we do not observe any significant filamentation for our cosmological initial conditions, and considering the relative simplicity of the 1D case, we will work in the untransformed phase space.

We now demonstrate the working of the Vlasov solver using some known tests. Note that since these standard tests are mainly in the context of plasma physics, the Poisson equation is the electrostatic one, and has an overall negative sign compared to the gravitational case. We start with the free-streaming Vlasov equation, where the potential $\phi(x, t) = 0$ (and therefore the Poisson equation need not be solved). For the initial condition

$$f(x, p, t_0) = \frac{A}{\sqrt{2\pi}} \exp\left(\frac{-p^2}{2}\right) \cos(nx) , \tag{3.23}$$

the discretised density given by

$$\rho(x, t) = \sum_{j=0}^{N-1} f(x, p_j, t)\Delta p , \tag{3.24}$$

is a periodic function with a period (recurrence time) $T_R = 2\pi/(n\Delta p)$. We reproduce Fig. 2 of [71] for the choice $n = 0.5$ and $\Delta p \approx 0.3225$ by plotting the maximum value of the density as a function of simulation time. The resulting plot is shown in Fig. 3.2.

To test the full Vlasov solver including the Poisson equation, we use the example of dissipation without collisions known as Landau damping. For the initial distribution given by

$$f(x, p, t_0) = \frac{1}{\sqrt{2\pi}} \exp\left(\frac{-p^2}{2}\right) [1 + A \cos(nx)] , \tag{3.25}$$

we plot the amplitude of the electric field $E \propto \nabla\phi_{\mathrm{E}}$ as a function of time in Fig. 3.3. Notice the initial linear fall in amplitude, followed by the jump after $t = 30$, and the recovery of recurrence near the theoretical time $T_R = 38.96$. This can be compared to similar tests in the literature, e.g. Fig. 4 of [74].

Finally, as a direct test of phase space evolution, we look at the two-stream instability – a plasma instability that can arise in two cold streams travelling in opposite directions due to wave-particle
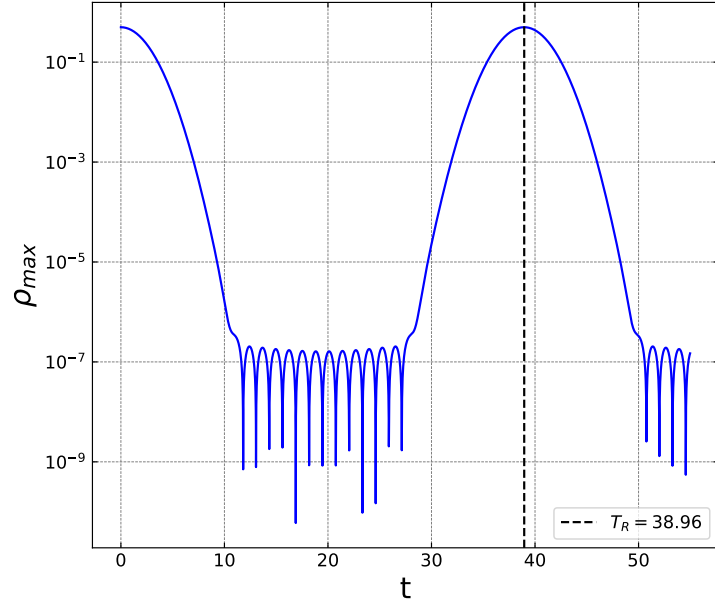
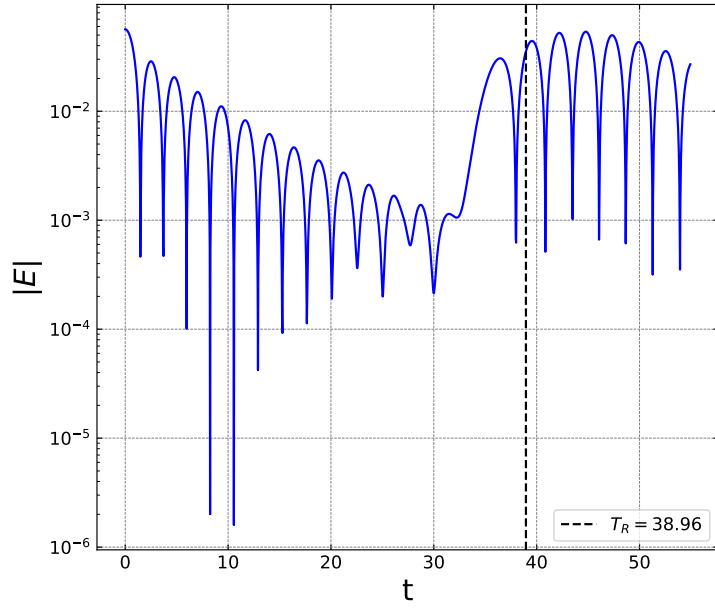Figure 3.2: The recurrence of the free streaming Vlasov solution.

Figure 3.3: The effect of Landau damping is apparent as the drop in amplitude of the electric field.

interactions. The initial condition for this instability is of the form

$$f(x, p, t_0) = \frac{1}{\sqrt{2\pi}} p^2 \exp\left(\frac{-p^2}{2}\right) [1 + A\cos(nx)] \ .$$

(3.26)

We plot the distribution f_V in phase space for three snapshots in Fig. 3.4. The qualitative behaviour of the system is as expected, as the two streams mix and form a vortex-like structure. In the last panel, the presence of filamentary structure can be observed, most notably towards both edges of the simulation box. The appearance of filamentation can be delayed by reducing the time-step, or smoothed out by filtration as previously discussed.

For a clearer direct comparison with the previous literature, we plot in Fig. 3.5 the time evolution of the total energy stored in the electric field, calculated in arbitrary units as $|E|^2/2$. This is in agreement with the previous works, e.g. Fig. 7 in [71], or Fig. 10 in [74].

It is important to note that these tests are all conducted on a nonexpanding grid, which corresponds to $a = 1$ in our system. Since we have an analytical solution in 1D – the Zeldovich approximation – we can ensure that our solver also works in the expanding universe with an evolving scale factor.
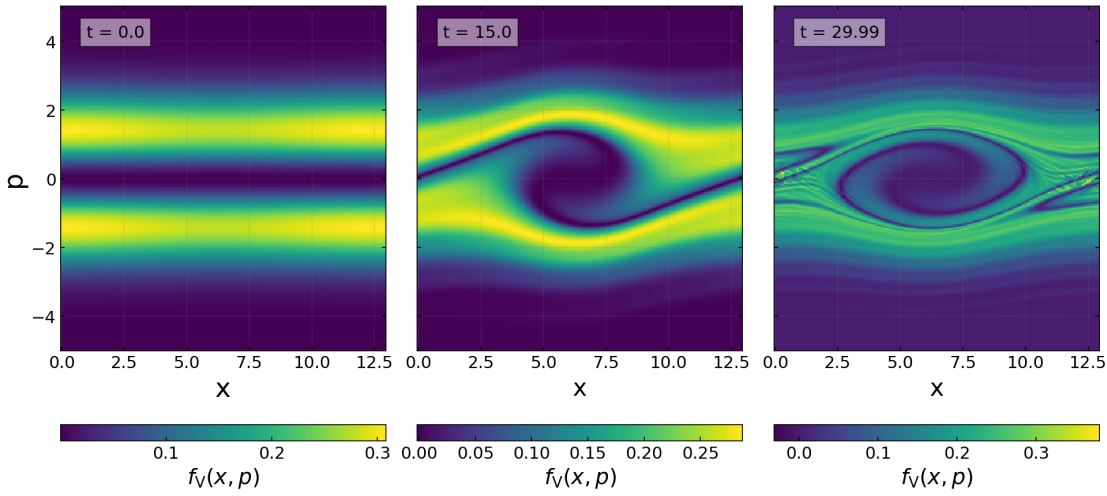
Figure 3.4: The evolution of two-stream instability.

3.3 Schrödinger Solver

The (time-dependent) Schrödinger equation is a nonlinear partial differential equation which can be written in a 1D expanding universe as

$$i\hbar \frac{\partial \psi(x,t)}{\partial t} = \left[-\frac{\hbar^2}{2ma^2} \frac{\partial^2}{\partial x^2} + m\phi(x,t) \right] \psi(x,t) . \tag{3.27}$$

The coupled 1D Poisson equation is

$$\frac{\partial^2 \phi}{\partial x^2} = \frac{3H_0^2}{2a} \left(|\psi|^2 - 1 \right) . \tag{3.28}$$

The right hand side of Eq. (3.27) defines the Hamiltonian H acting on ψ as

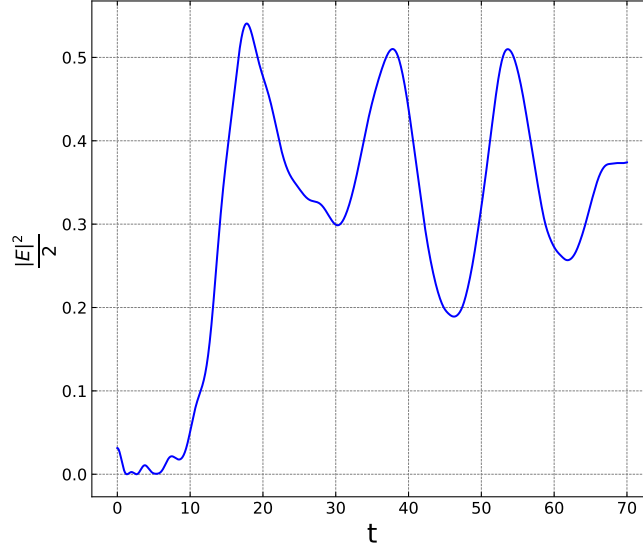$$H = -\frac{\hbar^2}{2ma^2} \frac{\partial^2}{\partial x^2} + \phi(x,t) . \tag{3.29}$$

Figure 3.5: Total electric field energy in the two-stream instability.

Thus, we can rewrite the Schrödinger equation in terms of H as

$$i\hbar \frac{\partial \psi(x,t)}{\partial t} = H\psi(x,t) \ . \tag{3.30}$$

The Hamiltonian represents the total energy of a given state of the system. We can treat Eq. (3.27) as a classical equation for the complex scalar field ψ, and $\hbar$ as a free parameter. The time dependence of the Hamiltonian comes from the potential $\phi(x,t)$ and the scale factor $a(t)$. If we discretise ϕ and a in time by assuming that they remain constant during a time-step Δt, we can write an analytical solution of the form

$$\psi(x, t + \Delta t) = \exp\left(-\frac{i}{\hbar}H\Delta t\right)\psi(x,t) \ . \tag{3.31}$$

Here, we can identify the time-evolution operator $U(\Delta t) = \exp(-iH\Delta t/\hbar)$ such that

$$\psi(x, t + \Delta t) = U(\Delta t)\psi(x,t) \ . \tag{3.32}$$

Thus, solving the Schrödinger equation amounts to evaluating $U(\Delta t)$ at each time-step, and then implementing its action on $\psi(x,t)$ to obtain $\psi(x, t + \Delta t)$. We can expand the exponential function in Eq. (3.31) in its infinite series to obtain

$$\psi(x, t + \Delta t) = \sum_{n=0}^{\infty} \frac{(-1)^n}{n!} \left(\frac{iH\Delta t}{\hbar}\right)^n \psi(x,t) \ . \tag{3.33}$$

A first order approximation to this yields an Euler method such that

$$\psi(x, t + \Delta t) = \left(1 - \frac{iH\Delta t}{\hbar}\right)\psi(x,t) \ , \tag{3.34}$$

which can then be solved by discretising in x. This method has global errors of order $O(\Delta t)$. Moreover, the method is unstable, and does not preserve the unitarity or time reversibility of $U(\Delta t)$. One way to improve upon this is to use an implicit scheme by writing

$$\psi(x, t + \Delta t) = \left(1 + \frac{iH\Delta t}{\hbar}\right)^{-1} \psi(x, t) \ . \tag{3.35}$$

Here, we can write H in matrix form and solve the resulting system by matrix inversion. This is called a *backwards* Euler method, and is more stable than the forward scheme. However, the method remains nonunitary and irreversible. To preserve these properties, the two Euler methods can be combined to obtain the following

$$\psi(x, t + \Delta t) = \frac{(2 - iH\Delta t/\hbar)}{(2 + iH\Delta t/\hbar)} \psi(x, t) \ . \tag{3.36}$$

This is known as the Crank-Nicolson approximation. It is both unitary and time reversible, and can be solved in matrix form by inversion. However, the computation involved may be expensive.

In this work, we use a split-operator method which makes the approximation

$$\exp\left(-\frac{i}{\hbar}H\Delta t\right) \approx \exp\left(-\frac{iT\Delta t}{2\hbar}\right) \exp\left(-\frac{iV\Delta t}{2\hbar}\right) \exp\left(-\frac{iT\Delta t}{2\hbar}\right) , \tag{3.37}$$

where

$$T = \frac{-h^2}{2ma^2} \frac{\partial^2}{\partial x^2} \ , \qquad V = m\phi \ , \tag{3.38}$$

are the kinetic and potential energy operators respectively. The matrix form of T is diagonal in momentum space, while that of V is diagonal in position space. Since the Fourier transform offers a way to transition between the two spaces, this method is simple to implement. It should be noted that the approximation in Eq. (3.37) is exact if the operators T and V commute, and thus the local error is proportional to $[T, V]$. Therefore, in general, the split-operator method has an error of order $O(\Delta t^2)$. Since part of the solution is obtained in Fourier (momentum) space, and part in real space, this method is classified as a 'pseudospectral' method [75, 76]. For a discussion of the various numerical techniques to solve the Schrödinger equation, see, e.g., [77, 78].

We will now sketch the algorithm for the split-operator method. Following [55], we start by changing the time variable to $\eta = \ln[a(t)]$. This allows us to rewrite Eq. (3.27) as

$$ih\frac{\partial \eta}{\partial t} \frac{\partial \psi}{\partial \eta} = -\frac{\hbar^2}{2ma^2} \frac{\partial^2 \psi}{\partial x^2} + m\phi\psi \ . \tag{3.39}$$

Using $\partial \eta / \partial t = H_0 a^{-3/2}$ and rearranging, we get

$$i\frac{\partial \psi}{\partial \eta} = -\frac{\hbar}{2mH_0 \sqrt{a}} \frac{\partial^2 \psi}{\partial x^2} + \frac{m}{hH_0 a^{-3/2}} \phi\psi \ . \tag{3.40}$$

We can thus write the SP equations

$$i\frac{\partial \psi}{\partial \eta} = -\frac{\kappa}{2} \frac{\partial^2 \psi}{\partial x^2} + \bar{\phi}\psi \ , \tag{3.41}$$

$$\frac{\partial^2 \bar{\phi}}{\partial x^2} = \frac{3}{2\kappa}\left(|\psi|^2 - 1\right) , \tag{3.42}$$

where

$$\kappa(\eta) = \frac{\hbar}{mH_0\sqrt{a}} , \qquad \bar{\phi} = \frac{m}{hH_0 a^{-3/2}}\phi . \tag{3.43}$$

In this setup, the Hamiltonian has the simple form

$$H = -\frac{\kappa}{2}\frac{\partial^2}{\partial x^2} + \bar{\phi} . \tag{3.44}$$

Therefore, the split-operator approximation becomes

$$\psi(x, \eta + \Delta\eta) = U_T\,U_V\,U_T\left[\psi(x, \eta)\right] , \tag{3.45}$$

where

$$U_T = \exp\left(i\kappa\frac{\Delta\eta}{4}\frac{\partial^2}{\partial x^2}\right) , \qquad U_V = \exp\left(-i\bar{\phi}\Delta\eta\right) , \tag{3.46}$$

are the time-evolution operators for the kinetic and potential parts respectively. Note that the global ordering of the operators U_T and U_V can be changed without introducing additional errors, i.e. $U_T\,U_V\,U_T \equiv U_V\,U_T\,U_V$ (Eq. 3.46 changes accordingly). On a discrete grid, this can be implemented in three steps as follows

$$\psi^*(x_j) = \mathcal{F}_x^{-1}\left\{\exp\left(-ik_x^2\kappa\frac{\Delta\eta}{4}\right)\mathcal{F}_x\left[\psi^n(x_j)\right]\right\} , \tag{3.47a}$$

$$\psi^{**}(x_j) = \exp\left(-i\bar{\phi}\Delta\eta\right)\left[\psi^*(x_j)\right] , \tag{3.47b}$$

$$\psi^{n+1}(x_j) = \mathcal{F}_x^{-1}\left\{\exp\left(-ik_x^2\kappa\frac{\Delta\eta}{4}\right)\mathcal{F}_x\left[\psi^{**}(x_j)\right]\right\} , \tag{3.47c}$$

where the superscripts n and $n+1$ correspond to times η_n and η_{n+1} such that their difference is $\Delta\eta$, and the starred superscripts refer to intermediate times not defined on the grid.

The construction of the Husimi distribution defined in Eq. (2.72, 2.73) can also be done using a Fourier transform. The 1D distribution is given as

$$f_H(x, p) = \left|\int dx' K_H(x, x', p)\psi(x')\right|^2 , \tag{3.48}$$

where

$$K_H(x, x', p) = \left(\frac{1}{2\pi\hbar}\right)^{1/2}\left(\frac{1}{2\pi\sigma_x^2}\right)^{1/4}\exp\left[-\frac{(x-x')^2}{4\sigma_x^2} - \frac{i}{\hbar}p\left(x' - \frac{x}{2}\right)\right] . \tag{3.49}$$

We can modify the kernel K_H slightly to obtain

$$K_H(x, x', p) = \left(\frac{1}{2\pi\hbar}\right)^{1/2}\left(\frac{1}{2\pi\sigma_x^2}\right)^{1/4}\exp\left(-\frac{ipx}{2\hbar}\right)\exp\left[-\frac{(x-x')^2}{4\sigma_x^2} + \frac{ip(x-x')}{\hbar}\right] . \tag{3.50}$$

Substituting this in Eq. (3.48), we get

$$f_{\mathrm{H}}(x, p) = \left| \left(\frac{1}{2\pi\hbar} \right)^{1/2} \left(\frac{1}{2\pi\sigma_x^2} \right)^{1/4} \exp\left(-\frac{ipx}{2\hbar} \right) \int \mathrm{d}x' G(x - x') \psi(x') \right|^2 , \tag{3.51}$$

where

$$G(x - x') = \exp\left[-\frac{(x - x')^2}{4\sigma_x^2} + \frac{ip(x - x')}{\hbar} \right] . \tag{3.52}$$

The integral thus defined in Eq. (3.51) is a convolution (usually denoted by '*'). Therefore, we can write

$$f_{\mathrm{H}}(x, p) = \left| A \exp\left(-\frac{ipx}{2\hbar} \right) (G * \psi)(x) \right|^2 , \tag{3.53}$$

where $A = (2\pi\hbar)^{-1/2} \left(2\pi\sigma_x^2 \right)^{-1/4}$. The convolution theorem of Fourier transforms tells us that the Fourier transform of the convolution of two functions is the product of their Fourier transforms (see, e.g., [79]). Therefore, the algorithm for computing f_{H} from ψ can be summarised as

$$f_{\mathrm{H}}(x, p) = \left| A \exp\left(-\frac{ipx}{2\hbar} \right) \mathcal{F}_x^{-1} \left[\mathcal{F}_x(G) \cdot \mathcal{F}_x(\psi) \right] \right|^2 . \tag{3.54}$$

We follow [57] in choosing a time-step criterion, by ensuring that the phase of the time-evolution operators in Eq. (3.46) is less than some maximum value $\theta_{\max}$. Therefore, we define two internal time-steps

$$\Delta\eta_1 = \frac{4\theta_{\max}}{\kappa k_{\max}^2} , \qquad \Delta\eta_2 = \frac{\theta_{\max}}{\bar{\phi}_{\max}} . \tag{3.55}$$

Then the smaller of these two is chosen as the time-step, i.e.,

$$\Delta\eta = \min\left(\Delta\eta_1, \Delta\eta_2 \right) . \tag{3.56}$$

We can now make a simple test of the solver built from the above algorithm. We assume a nonexpanding universe (such that $a = 1$, and κ is constant) without an external potential. The Hamiltonian in such a universe is

$$H = -\frac{\kappa}{2} \frac{\partial^2}{\partial x^2} . \tag{3.57}$$

Using Eq. (3.47), we see that this system has an analytical solution of the form

$$\psi(x, \eta) = \mathcal{F}_x^{-1} \left[\exp\left(-ik_x^2 k\eta \right) \widetilde{\psi}(x, 0) \right] , \tag{3.58}$$

where $\widetilde{\psi}(x, 0) = \mathcal{F}_x[\psi(x, 0)]$. Consider the initial condition

$$\psi(x, 0) = \left(\frac{1}{2\pi\sigma} \right)^{1/2} \exp\left[-\frac{(x - x_0)^2}{2\sigma^2} + ik_0 x \right] , \tag{3.59}$$

where σ and x_0 are the variance and the mean of the Gaussian in x, and k_0 is some initial momentum. In Fig. 3.6, we plot the density $\rho = |\psi|^2$ from the analytical and numerical solutions for the initial conditions and at a later time, and observe that they coincide as we expect. We also plot the fractional difference between the analytical and numerical solutions scaled by the analytical density in the lower panels of Fig. 3.6.
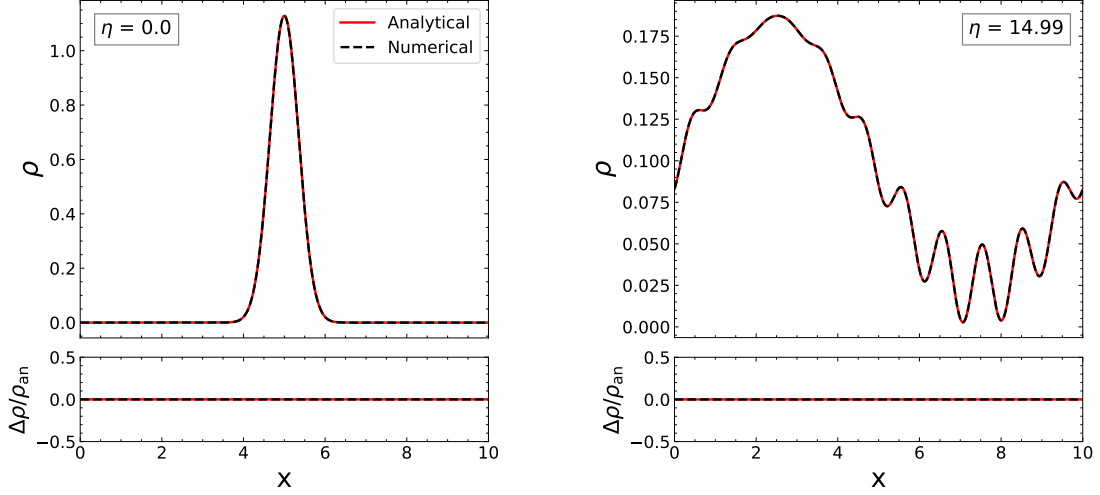

Figure 3.6: Test of the free-particle Schrödinger equation with initial parameters $\sigma = 0.5$, $x_0 = k_0 = 5$. The lower panels indicate the fractional difference between the two solutions.

3.4 N-body simulations with `GADGET-2`

To serve as a standard test of our methods after shell crossing, we use the cosmological simulation code `GADGET-2` [1]. The dynamics is fully contained in the Hamiltonian $H(x, p)$ defined as

$$H = \sum_i \frac{p_i^2}{2ma^2(t)} + \frac{1}{2} \sum_{ij} \frac{m_i m_j \Phi(x_i - x_j)}{a(t)} \,, \tag{3.60}$$

where Φ is the interaction potential. It is obtained by solving the Poisson equation of the form

$$\frac{\partial^2 \Phi}{\partial x^2} = 4\pi G \left[\sum_j \bar{\delta}^D (x - jL) - \frac{1}{L} \right] \,, \tag{3.61}$$

where $\bar{\delta}^D(x)$ is a Dirac delta smoothed with a softening length ϵ. The algorithm used for force computation is a hybrid TreePM method. To calculate the force on any given particle, the computational domain is divided into cells. The nearest particles are grouped in small cells, and this cell size scales with distance from the particle. The peculiar gravitational potential is split into short-range and long-range components, where the former is evaluated using the tree algorithm, and the latter using a PM method. To carry out the time integration, a leapfrog scheme is implemented. The details of this are similar to the split-operator method described in the previous section. The Hamiltonian is split

into kinetic and potential parts, and the time-evolution operator takes the form

$$U(\Delta t) = U_V \left(\frac{\Delta t}{2}\right) U_T (\Delta t) \, U_V \left(\frac{\Delta t}{2}\right) , \tag{3.62}$$

where U_T and U_V represent the kinetic and potential parts respectively. Following the TreePM approach, the potential part is further separated into short and long range operators, so that the overall scheme is given as

$$U(\Delta t) = U_V^l \left(\frac{\Delta t}{2}\right) \left[U_V^s \left(\frac{\Delta t}{2}\right) U_T (\Delta t) \, U_V^s \left(\frac{\Delta t}{2}\right) \right] U_V^l \left(\frac{\Delta t}{2}\right) , \tag{3.63}$$

where the superscripts s and l refer to short and long range respectively. The time-step is adaptive, such that $\Delta t \propto (|g|)^{-1/2}$ where g is the acceleration during the previous time-step. The proportionality constant depends on the softening length.

`GADGET-2` is written for 3D simulations. To simulate our 1D universe, we use plane-parallel initial conditions. Assume that the initial (Lagrangian) coordinates are given by (q_1, q_2, q_3), and the corresponding particle velocities by (u_1, u_2, u_3). The initially cold setup is perturbed along one direction using the Zeldovich approximation (1LPT) to $a = 0.1$. At this time, the position along that dimension is then the Eulerian coordinate (say x_1) given by

$$x_1 = q_1 + s(q_1, a) , \tag{3.64}$$

where $s(q_1, a)$ is the 1LPT displacement field, and the velocity is given by

$$v_1 = \dot{a} u_1(q_1) . \tag{3.65}$$

The velocity along the other directions is set to zero. Thus, the initial position and velocity vectors for the simulation take the form

$$\mathbf{x}_{\text{in}} = (x_1, q_2, q_3) , \qquad \mathbf{v}_{\text{in}} = (v_1, 0, 0) . \tag{3.66}$$

This generates a series of parallel planes in the 3D box, such that the dynamics in each plane is purely 1D (or 2D in phase space). Using LPT to evolve the linear dynamics at higher redshifts is standard practice in cosmological simulations. It has been argued that using lower order LPT may lead to systematic errors in the nonlinear regime, and that using third-order LPT (3LPT) is sufficient to reduce these errors [80]. However, this does not affect us since our simulations are effectively 1D where 1LPT is exact.

For specified redshifts, the code returns 'snapshots' of the simulation, which are files that contain the state of the system at that redshift. The positions and velocities of DM particles can then be extracted from these files. The default file format for the initial conditions as well as the snapshots is binary, but the code also supports the hierarchical data format (HDF). The code allows modifications to parameters that determine accuracy, integration time, the choice of comoving grid, and so on. Details on these parameters can be found in [81].

Until now, we have introduced four different models that we can use to probe DM dynamics, viz., the VP equations, PT (the dust model), the SP equations, and N-body simulations. We have set up the methods by which we can solve these models, leaving us in a position to analyse our 1D universe in all

of them. In the following chapter, we present and discuss the results obtained from this analysis.

Results and Discussion

4.1 Initial Conditions

The overdensity field completely specifies the initial conditions for all our models. The Lagrangian overdensity is chosen to be

$$\delta_0(q) = -d_0 \cos(q) \, . \tag{4.1}$$

The resulting displacement field in the 1LPT framework is then given by

$$s(q, a) = a \, d_0 \, \sin(q) \, . \tag{4.2}$$

This allows us to calculate the Eulerian position

$$x(q, a) = q + a \, d_0 \sin(q) \, , \tag{4.3}$$

the 1LPT overdensity field

$$\delta_{1\text{LPT}}(x, a) = \left| 1 + a \, d_0 \cos(q) \right|^{-1} - 1 \, , \tag{4.4}$$

and the velocity field

$$v_{1\text{LPT}}(x, a) = \sqrt{a} H_0 d_0 \sin(q) \, . \tag{4.5}$$

We set $d_0 = 0.5$. We begin our simulations at $a_{\text{in}} = 0.1$, when the overdensity is given as

$$\begin{aligned} \delta(x, a_{\text{in}}) &= |1 + 0.05 \cos(q)|^{-1} - 1 \\ &\approx 0.05 \cos(q) \end{aligned} \tag{4.6}$$

The first shell crossing will occur at $a = 2$. Fig. 4.1 shows the overdensity and velocity fields at $a = 0.1$. The overdensity peak is located at the centre of the box. The phase space plot shows that the velocity is single-valued everywhere. This is the single-stream regime where the assumption $\sigma_{ij} = 0$ holds. To obtain the initial conditions for the SP system, we use the Madelung representation (Eq. 2.64). For calculating the velocity potential that enters its phase, we solve the Poisson equation for the initial overdensity. The resulting gravitational potential yields the velocity potential using Eq. (2.51). From the initial ψ, we can construct the corresponding Husimi distribution (from Eq. 2.72, Eq. 2.73)
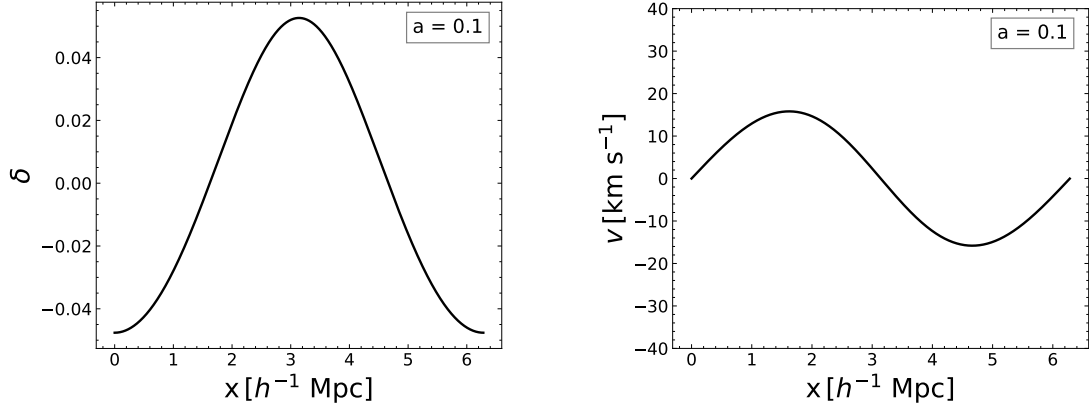
Figure 4.1: 1LPT overdensity and velocity fields at $a = 0.1$, obtained from Eq. (4.4), Eq. (4.5) respectively.

Table 4.1: Parameters of the SP and VP solvers.

	Boxsize [h^{-1} Mpc]	Number of grid points	Δa	$\hbar$ [M_{10} Mpc km s^{-1} h^{-2}]	σ_x [Mpc]
SP	2π	4096	adaptive	0.03	0.03
VP	2π	4096	0.005	0.03 (ICs)	0.03 (ICs)

Table 4.2: Parameters of the N-body run.

	Boxsize [h^{-1} Mpc]	Particle number (per dimension)	Δt_{max}	Softening length [h^{-1} Mpc]
N-body	2π	200	0.05	5×10^{-6}

which serves as the initial condition for the VP solver. The details of the SP and VP simulations are given in Table 4.1[1]. Details of the GADGET-2 run are provided in Table 4.2.

4.2 General behaviour in the linear regime

We will demonstrate the general behaviour of the models via plots of the overdensity field δ, and the velocity field v. The overdensity peak causes the particles to fall towards the centre resulting in growth of the central overdensity. At early times $a < 1$, the overdensity grows linearly with a. We show this linear evolution in the SP, VP, and 1LPT models in Fig. 4.2. The bottom row shows the fractional difference between each model and the exact solution of 1LPT. All three methods show the same general evolution. The overdensity peaks nearly coincide at early times (left column of Fig. 4.2), but deviations appear after $a > 1$ (central column). The SP overdensity at the centre is smaller than the exact 1LPT solution, and the VP overdensity is even smaller. The suppression in SP overdensity as compared to 1LPT is likely a consequence of the smoothing scales ($\hbar$ and σ_x) inherent in SP, but the difference is harder to explain in the VP case. Since the VP solver is a phase-space code,

---

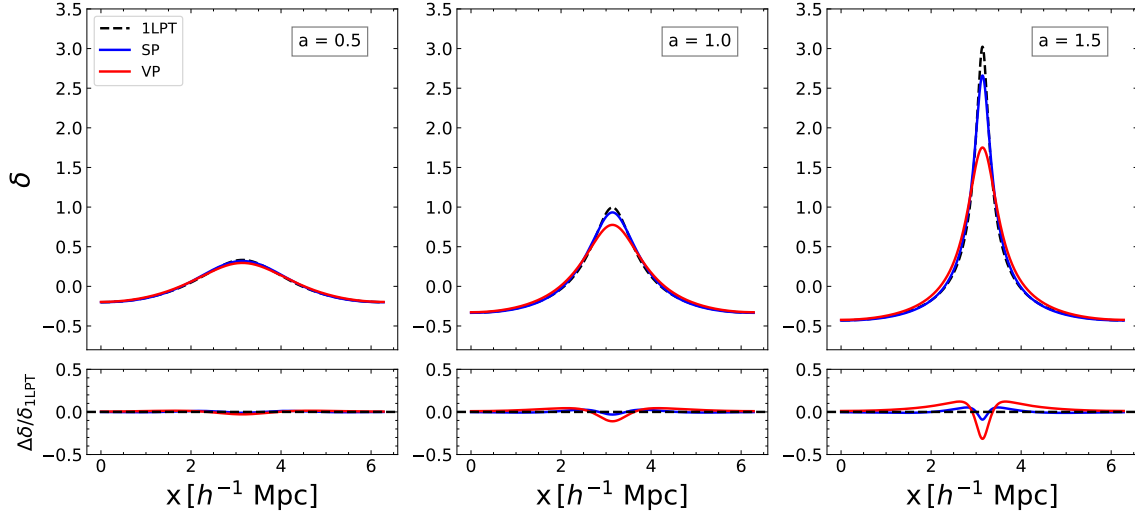[1] The unit of mass $M_{10} := 10^{10}\,M_\odot$ is also the default unit in GADGET-2.

Figure 4.2: The behaviour of the SP, VP, and 1LPT overdensity before shell crossing. The models show agreement at early times, but the SP and VP central overdensity deviates from 1LPT after $a \geq 1$.

this suppression may reflect the lack of phase-space resolution, especially close to the centre. The difference is amplified as a increases as seen in the right column of Fig. 4.2.

Fig. 4.3 shows the phase space plots before shell crossing. The colour plot is obtained from the 2D Husimi distribution (f_H) constructed after solving the SP equations, and we overplot the 1LPT and N-body velocities. The velocity at the centre of the box is zero. In both directions away from the centre, the absolute value of the velocity increases till it reaches a maximum, and then falls off towards the edge of the box. Thus, the particles approach the overdensity peak at the centre from both sides. Before shell crossing, they constitute a single coherent flow. Any line drawn parallel to the velocity axis only intersects one part of the phase-space sheet, and we are in the single-stream regime. The particles continue to fall towards the centre, and the sheet starts to bend under the influence of gravity. Close to shell crossing (bottom right panel of Fig. 4.3), the phase-space sheet is nearly vertical. The value of the distribution f_H is a measure of phase-space density. The orange and yellow in the colour plot indicate a larger value, pointing to a higher density close to the centre. On average, these values increase with time as the particles with high densities and momenta move towards the centre.

4.3 Shell-crossing singularity

At $a = a_{sc}$[2], the two streams of infalling matter meet at the centre of the box, and the overdensity formally goes to infinity. This is the instant of first shell crossing. The location of the first shell crossing coincides with the location of the peak in the initial density, i.e., $x_{sc} = \pi \, h^{-1}$Mpc. Fig. 4.4 shows the overdensity field at a_{sc} for the 1LPT, SP and VP solutions. The SP overdensity follows that of 1LPT in the outer regions but overpredicts close to the centre as seen in the fractional difference in the second row of Fig. 4.4. The finite central overdensity in SP is a consequence of the regularisation that $\hbar$ induces. In the VP solution, we observe larger deviations from 1LPT away from the centre,

---

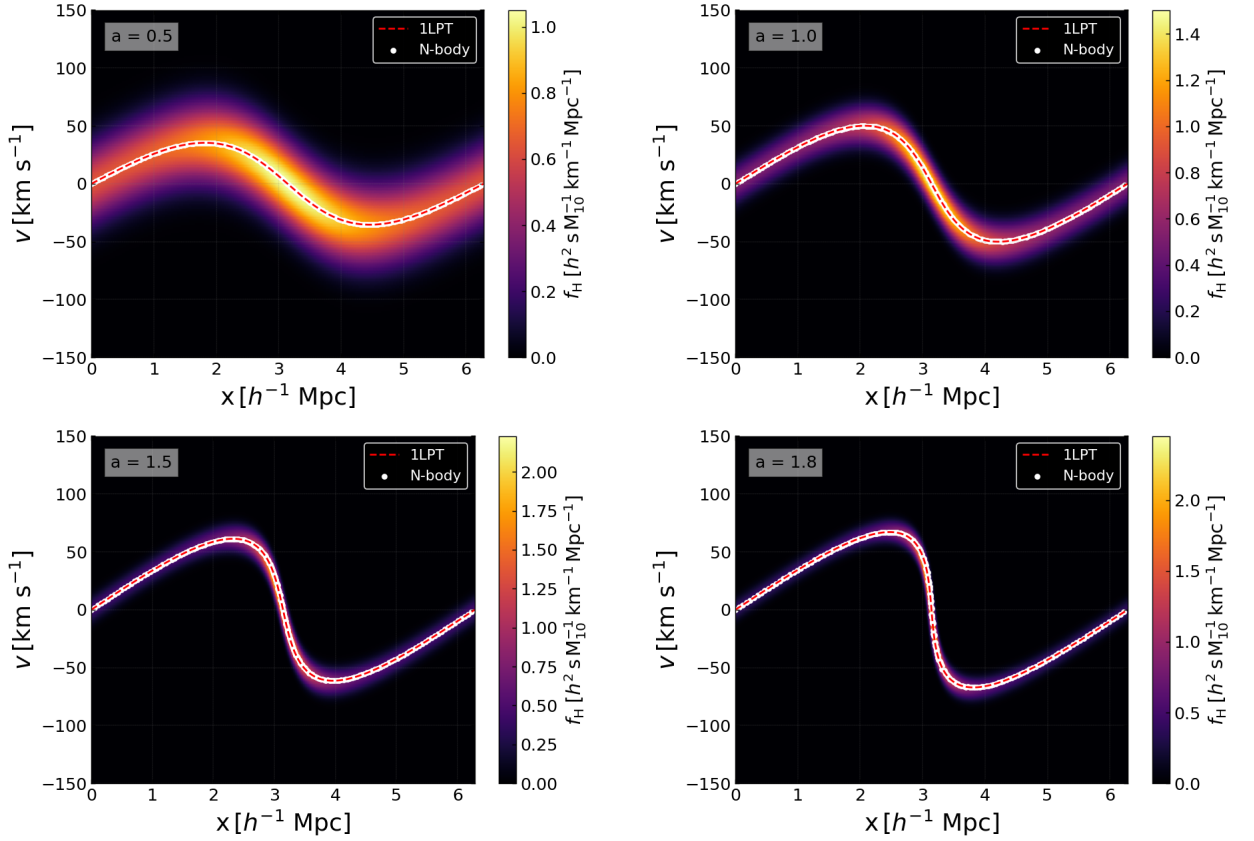[2] The subscript 'sc' refers to shell crossing.

Figure 4.3: Comparison between the 1LPT (dashed red line), SP (coloured plot), and N-body (white points) models in phase space before shell crossing.

where it also overpredicts the overdensity.

Fig. 4.5 shows the phase-space sheet at shell crossing for the 1LPT, SP and N-body solutions. The trajectories of the particles approaching the centre from both sides are crossing at this instant, making the phase-space sheet vertical. The velocity gradient diverges at x_{sc}, corresponding to the overdensity singularity. The value of the distribution function reaches a turning point close to shell crossing. In Fig. 4.3, we saw that this was increasing with time. Slightly before $a = 2$, this trend reverses, and we see a small decline until shell crossing, after which it starts increasing again.

4.4 Breakdown of the dust model

We now demonstrate the breakdown of the dust model in both the Eulerian (SPT) and Lagrangian (1LPT) pictures. 1LPT is exact until shell crossing, but does not give physical results after shell crossing. To compare the differences between SPT and 1LPT, we plot the overdensity and velocity fields in the two frameworks. For SPT, we show the fourth (4SPT) and eighth order (8SPT) solutions. Fig. 4.6 shows the evolution of the overdensity field. The bottom row plots the fractional difference between SPT and 1LPT scaled by 1LPT, such that a value of zero indicates complete agreement between the solutions. At an early time $a = 0.4$, (left panel of Fig. 4.6), the two SPT solutions agree
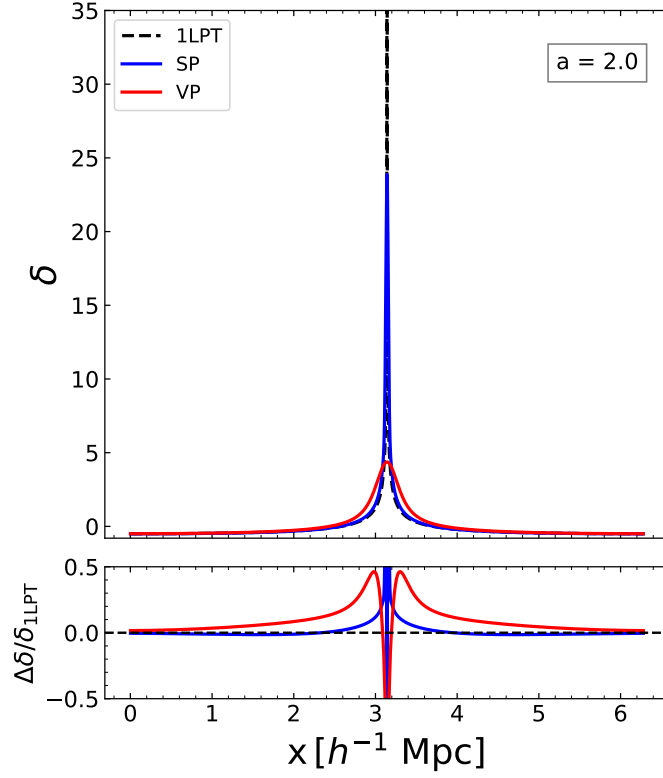
Figure 4.4: The overdensity plot at shell crossing ($a = 2$). 1LPT develops a central singularity, while the SP and VP overdensities remain finite. The SP matches 1LPT away from the centre, but the VP overdensity does not.
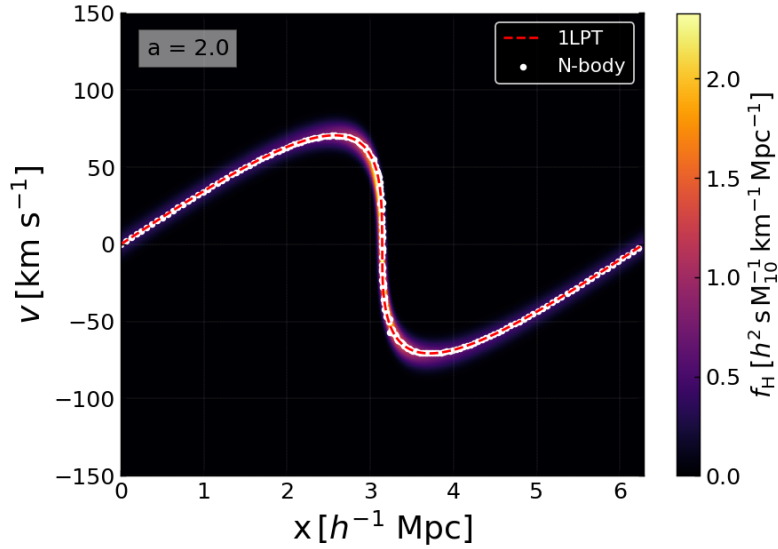

Figure 4.5: The phase-space plot at shell crossing ($a = 2$). The phase-space sheet is parallel to the velocity axis, and the velocity gradient becomes infinite.
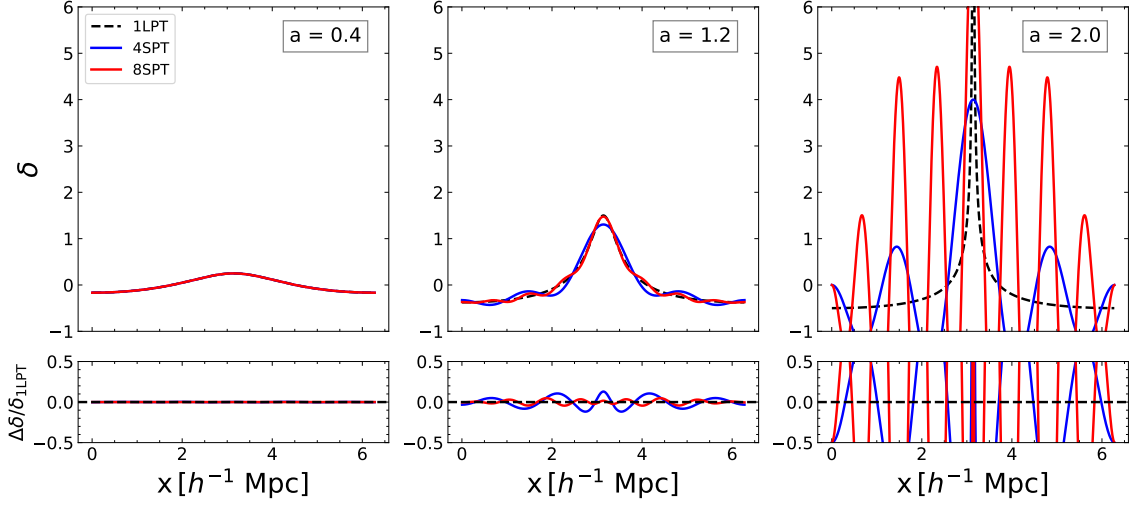
Figure 4.6: Comparison between LPT (dashed black line) and SPT (red and blue lines) overdensity field. At early times, the two SPT solutions agree with 1LPT (left panel). SPT starts to deviate from the exact solution closer to shell crossing (central panel), with 8SPT performing better than 4SPT. However, both SPT solutions become highly oscillatory by the epoch of shell crossing (right panel).

with 1LPT, and the three lines coincide. In the middle panel ($a = 1.2$), we see that SPT deviates from 1LPT. Both 4SPT and 8SPT oscillate about the exact solution. Between the two SPT solutions, 8SPT shows milder oscillations at $a = 1.2$, and better agreement with 1LPT. However, the oscillations grow with a, and by the epoch of first shell crossing (right panel of Fig. 4.6), the overdensity becomes unphysical.

To understand where these oscillations originate, we can take another look at SPT density kernels, e.g., Eq. (2.45). In Section 2.2.1, we saw that the density in n^{th} order SPT will contain terms proportional to $\delta_0^n(x)$. In other words, the higher order terms in the SPT expansion contain large powers of the initial overdensity, which is a cosine wave. These terms become more important as a increases, and give rise to the oscillations we see. This is supported by the fact that 8SPT shows more oscillatory behaviour than 4SPT at later times, as shown in the right panel of Fig. 4.6. At the instant of shell crossing, $\delta < -1$ in certain regions of the box, which is unphysical.

The same behaviour can be seen in the phase space plots in Fig. 4.7. The nth order velocity term in SPT is the gradient of the overdensity term of that order. SPT and 1LPT agree on their velocities in the linear regime (left panel of Fig. 4.7), and the lines coincide. In the central panel ($a = 1.2$), we see deviations from the exact solution. The 8SPT solution shows milder oscillations and better agreement with 1LPT, similar to what we observed in the overdensity plots. At shell crossing (right panel of Fig. 4.7), we see large oscillations, which are more extreme in the 8SPT solution.

The above results show that the Eulerian solution of the dust model (SPT) stops making correct predictions *before* shell crossing. The 1LPT overdensity field becomes singular *at* shell crossing. As discussed in Section 2.2.2, this singularity only appears at the instant of shell crossing, after which the central density becomes finite again. Nonetheless, the assumption of the dust model that $\sigma_{ij} = 0$ is no longer valid after shell crossing, and LPT does not make meaningful predictions after this. It was found in [82] that the shell-crossing singularity does not limit the convergence of the LPT series,
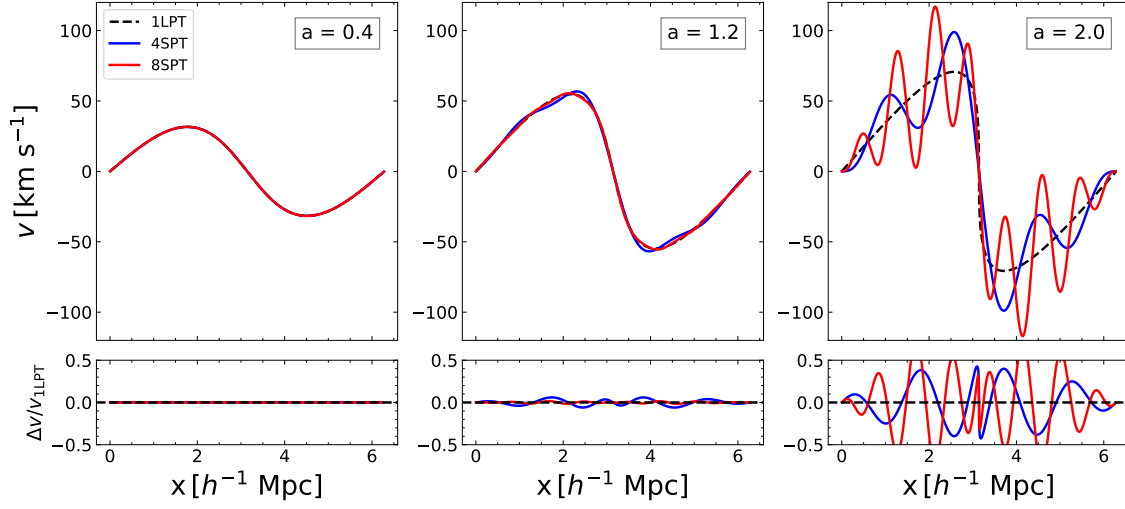
Figure 4.7: Comparison between LPT (dashed black line) and SPT (red and blue lines) velocities. The left panel shows reasonable agreement at earlier times ($a = 0.4$). The central panel shows the emergence of oscillatory behaviour, which becomes extreme by the epoch of shell crossing (right panel).
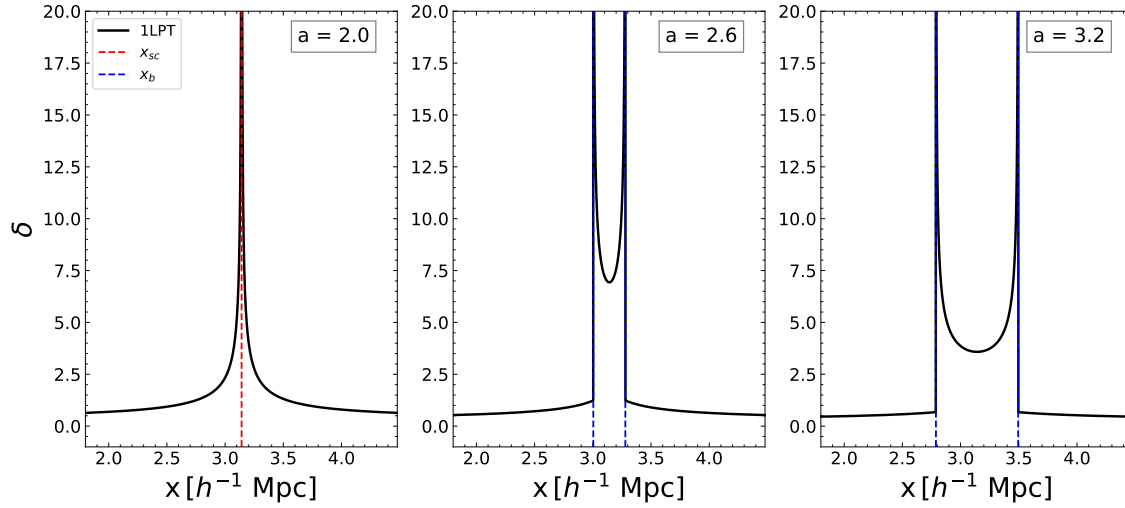

Figure 4.8: Overdensity after shell crossing in 1LPT. The central density is instantaneously singular at $a = 2$, then becomes finite. Two singularities then emerge at the boundaries of a pancake region where all structure is smeared out (shown in blue dashed lines).

which remains convergent until shortly after shell crossing. In Fig. 4.8, we show the behaviour of the 1LPT overdensity after shell crossing. In the left panel, the central density is singular. Afterwords, the particles (or fluid elements) whose trajectories have just crossed continue to move in the same direction, forming a 'pancake' region where the overdensity remains finite, but all features are smeared out. The boundaries of this region (blue dashed lines) are points of a singularity different from a shell-crossing singularity. This pancake continues to grow indefinitely, and there is no recollapse.

4.5 Dynamics beyond shell crossing

4.5.1 Multistreaming

The SP system remains valid after shell crossing, and provides insight into dynamics after the dust model has broken down. First, we look at the overdensity field. Fig. 4.9 shows the 1LPT, SP and VP overdensities at three different times after shell crossing (from here on, we zoom in to the central region of the box to better see the structure). The particles whose trajectories crossed at a_{sc}, continue moving in the same direction. In 1LPT, the pancake structure grows faster as there is no turnaround. At $a = 3$ (left panel of Fig. 4.9), the location of the pancake boundary is still approximately the same in SP and 1LPT. The boundary corresponds to the particles involved in the first shell crossing. These particles form local density peaks either side of the centre. Between these two peaks, the SP overdensity has a highly coarse-grained structure, which is the combined action of $\hbar$ and σ_x. The VP overdensity is smoother, but does not match the amplitude of the SP overdensity peaks. In both SP and VP solutions, we observe a third density peak emerging at the centre. For VP, this is only visible in the middle panel ($a = 4.5$). This new peak grows until $a \approx 5.3$ (right panel) where the trajectories of the particles approaching each other from either side cross, leading to a second shell crossing. These particles then continue to move in the same direction, creating two more local density peaks, and this process will repeat.

In Fig. 4.10, we show the phase-space plots after shell crossing. In concert with the overdensity field, the phase-space sheet also expands after the first shell crossing as the momentum of the particles carries them away from the centre. The local overdensity peaks correspond to different streams in phase space. This is always an odd number, equal to one more than twice the number of shell crossings the system has undergone. The central peak that emerges in the overdensity field is accompanied by a further twist in the phase-space sheet. As this peak grows, this twist grows closer to being vertical (parallel to the velocity axis). In the bottom right panel of Fig. 4.10, we observe the second shell crossing. By this time, some particles in the N-body solution start to show spurious discreteness effects. This is because of the low number of particles used in the simulation, and a relatively large softening length. The phase-space density increases after the first shell crossing, reaches a maximum when the central part of the phase-space sheet is horizontal (perpendicular to the velocity axis), then starts decreasing again until the second shell crossing.

4.5.2 Late-time evolution

We can continue the evolution of the Schrödinger field ψ for a longer time. The resulting overdensity field is show in Fig. 4.11. The left panel shows the time after the second shell crossing with five local overdensity peaks. This corresponds to five streams in phase-space. The middle panel shows seven local peaks, meaning that the third shell crossing has already occurred. Finally, the right panel shows nine peaks, indicating that there have been four shell crossings before this time. The peaks which were formed last are quite close to the center. We show the corresponding phase-space plots in Fig. 4.12. The phase-space structure contracts as the system moves towards relaxation. This is accompanied by a tightening of the spiral structure along the position axis. The outermost 'arms' of this spiral have a very low phase-space density, especially at $a = 31.73$ (bottom row of Fig. 4.12) where the outermost arms are nearly invisible. At this time, the three innermost density peaks are quite close to one another. However, it is unclear whether this forms a single structure in a steady state.
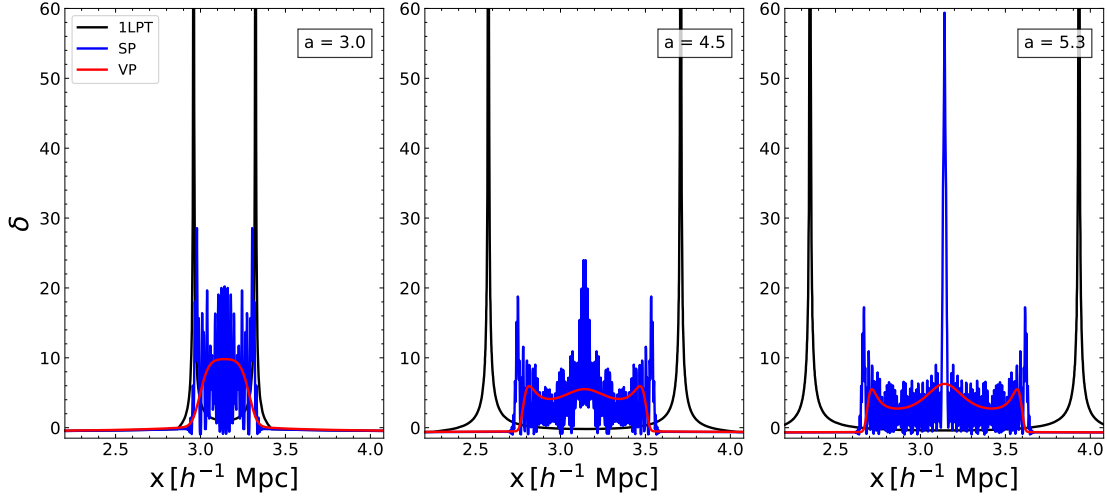
Figure 4.9: Evolution of the overdensity field after shell crossing. The boundaries of the central region in 1LPT (black line) continue expanding, while in the SP (blue line) and VP (red line) case, there is formation of another central density peak, followed by a second shell crossing.
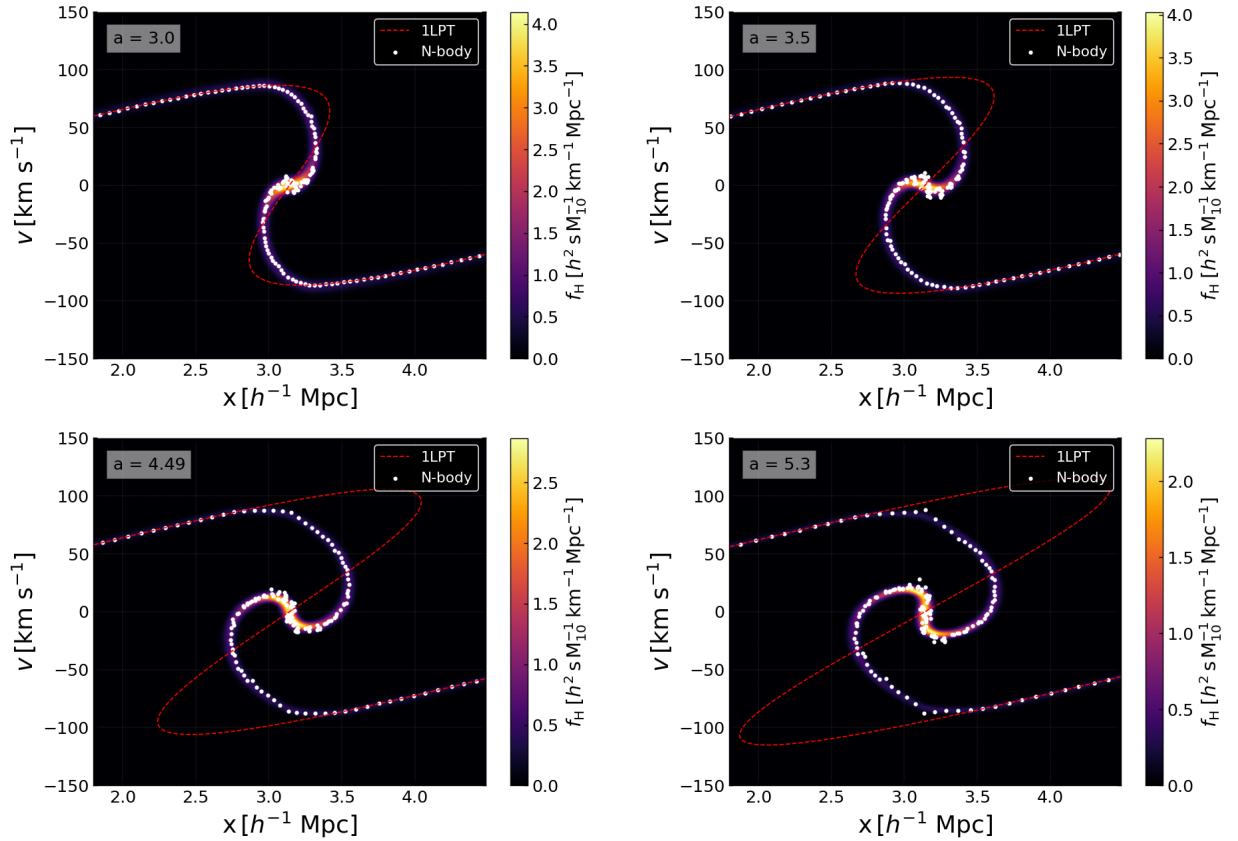

Figure 4.10: Multistreaming in phase space in SP (color plot) and N-body (white points) solutions. The 1LPT velocity is no longer correct, but the SP and N-body velocities are in agreement with each other.
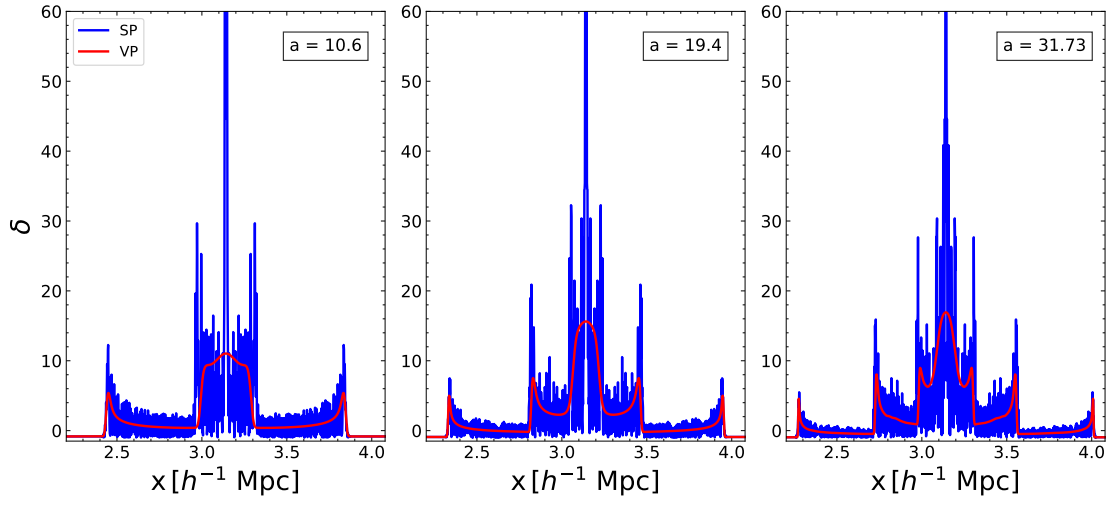
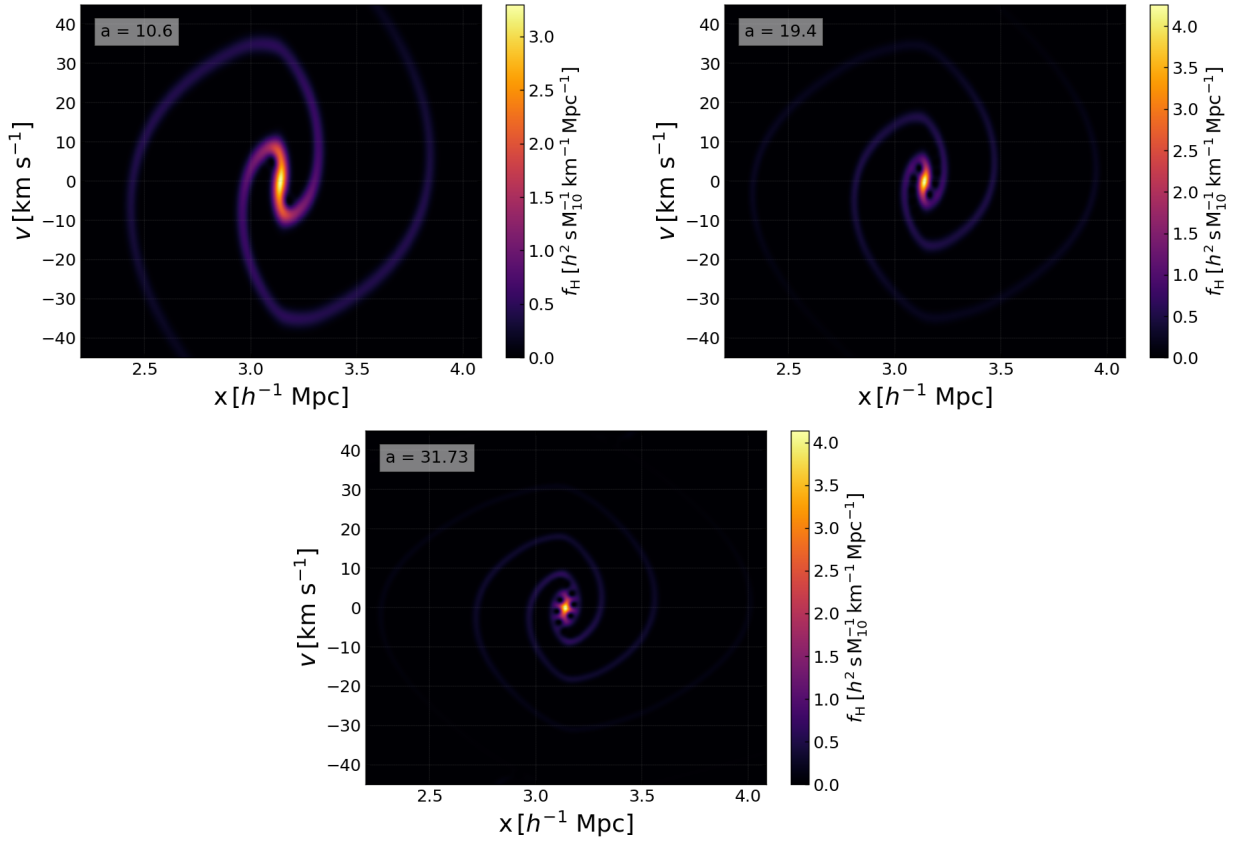Figure 4.11: Evolution of the overdensity field at a late time.

Figure 4.12: Late-time evolution in phase-space from the SP solution. We observe a contraction of the phase-space structure.

4.5.3 Effect of smoothing in SP

The SP system contains two smoothing scales – $\hbar$ and σ_x (the latter not to be confused with velocity dispersion σ). We vary these two scales and observe the effect this has on the overdensity field. In Section 4.5.1, we point out that the fluctuating features that appear in the overdensity field after shell crossing are a consequence of the coarse graining introduced by the smoothing scales. We demonstrate this effect in Fig. 4.13, where we plot the overdensity field for three different values of $\hbar$, and three different choices of σ_x at the same time $a = 5.5$. This was chosen to be after the second shell crossing. As we move from left to right in the plot, the value of $\hbar$ increases. We see that this reduces the amount of coarse graining in the overdensity field. The value of the spatial smoothing scale σ_x increases from top to bottom. As expected, a larger value smoothes out more structure. The value of σ_x has to be changed by an order of magnitude before visible changes in the overdensity appear, but it is more sensitive to changes in $\hbar$. Here, tt is important to stress that $\hbar$ is chosen at the beginning of the simulation, and must be the same for each solution set. However, solution of the Schrödinger equation does not require specifying σ_x. The latter is specified only when calculating the moments either by integrating over the Husimi distribution, or via the prescription described in Section 2.4. The Wigner moments do not require a spatial smoothing scale, and hence are only limited in resolution by $\hbar$. Overall, $\hbar$ *allows* more coarse graining, leading to more oscillations after shell crossing, and a choice of σ_x determines the scale on which these oscillations are smoothed out.

4.5.4 Velocity dispersion in SP

We can measure the velocity dispersion (σ) in the SP system using Eq. (2.95). In Fig. 4.14, we show the time evolution of the velocity dispersion at the centre of the box. For comparison, we also plot this evolution at the boundary of the box. At early times, σ is close to zero, agreeing with the predictions of the dust model. This continues to be the case until about $a = 1.5$ when σ becomes nonzero, but remains small. After the first shell crossing at $a = 2$, the value of σ starts rising at the centre of the box, accompanied by strong fluctuations characteristic of the coarse-graining by $\hbar$. At the edge of the box, σ remains zero throughout the evolution, except for small oscillations about zero at late times. Thus the assumption of the dust model that $\sigma = 0$ is invalid after shell crossing. Even with cold initial conditions, the system develops a nonzero velocity dispersion which cannot be ignored after shell crossing.
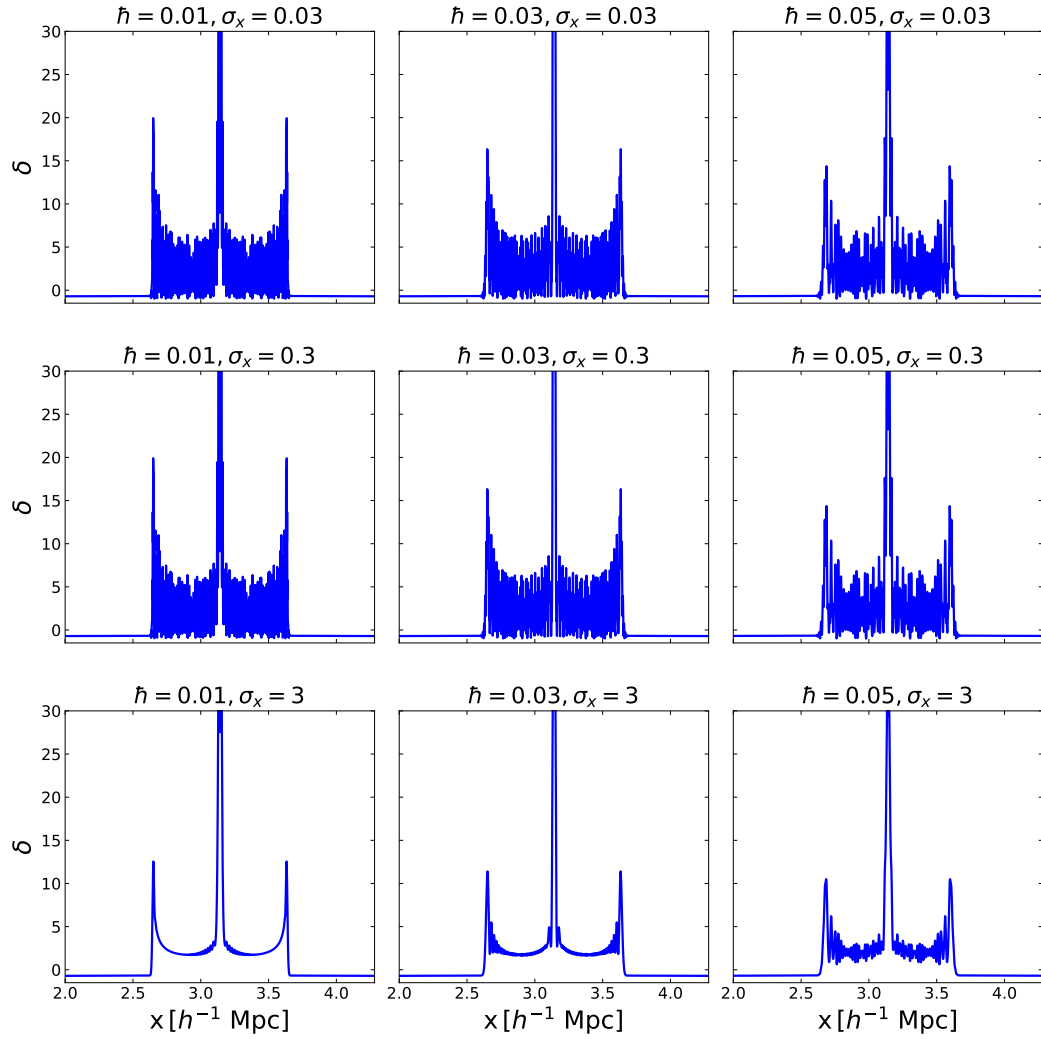
Figure 4.13: The effect of $\hbar$ (in units of $\mathrm{M_{10}\,Mpc\,km\,s^{-1}\,h^{-2}}$), and σ_x (in units of h^{-1} Mpc) on the overdensity field at $a = 5.5$.
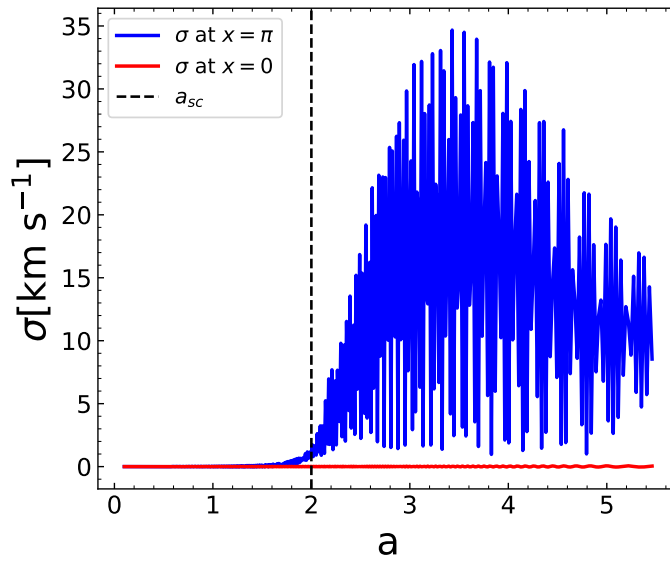
Figure 4.14: Evolution of the velocity dispersion at the centre (blue line) and the edge (red line) of the box in the SP system as a function of time. At the centre, σ remains zero at early times, but becomes large after shell crossing.

Conclusions

5.1 Summary

We began this work with the goal of studying different methods of modelling the behaviour of CDM under a gravitational potential. In a simplified 1D EdS universe for an initially sinusoidal overdensity, we studied four such methods, by comparing their predictions of the overdensity and velocity fields. First, we solved the VP system directly. Next, we looked at the standard approach in large-scale structure theory, i.e., use of the hierarchy of moments of the Vlasov equation, and the truncation of this hierarchy at second order via the single-stream approximation to yield the dust model. We solved the dust model in both Eulerian and Lagrangian frameworks. We also considered an alternative prescription – the coupled SP equations for a classical scalar field. We solved these equations in our 1D universe for initial conditions consistent with our other methods. Finally, we used the numerical code `GADGET-2` to run an N-body simulation. From our analysis of these models, we make the following remarks:

- All models show reasonable agreement in the linear regime, where $|\delta| \leq 1$.

- In the mildly nonlinear regime, where $\delta > 1$, the SPT solution begins to show oscillatory behaviour, especially for its lower order solutions. The SP overdensity at the centre of the box shows a mild suppression compared to the exact solution (1LPT). This is an expected consequence of the smoothing in SP. The VP solution shows a larger suppression and does not match the exact solution. This is likely due to an inaccurate solver. The 1LPT, SP, and N-body velocities show good agreement in both the linear and the mildly non-linear regime.

- As we enter the nonlinear regime and $\delta \gg 1$, the oscillations in the SPT soultions become extreme, signalling the breakdown of this approach. The eighth-order solution has more extreme oscillations compared to its fourth-order counterpart. At the instant of first shell crossing, the overdensity field in 1LPT becomes formally infinite. Although this singularity is only temporary, and although the perturbative expansion of LPT does not involve the overdensity field (but the displacement field), the first shell crossing marks the instant where 1LPT stops making meaningful predictions. The first shell crossing is accompanied by the appearance of nonzero velocity dispersion, and the dust model becomes invalid. The overdensity field in SP is finite, due to regularisation by $\hbar$. The VP overdensity is also finite, but does not match SP

exactly. At shell crossing, the phase-space sheet becomes parallel to the velocity axis. There are no singularities in phase space, and the 1LPT, SP, and N-body velocities continue to show agreement until shell crossing.

- After shell crossing, the system starts to become nonlinear on progressively larger scales. The trajectories of the particles involved in the first shell crossing continue in the same direction, seen as an expanding pancake-like structure in the overdensity field. In 1LPT, the boundaries of this pancake expand indefinitely, smearing out any structure in multistreaming regions. In SP and VP, this expansion is slower due to gravity. Along with the local density peaks that form at the pancake boundary, there is a third density peak at the centre, which grows with time leading to a second shell crossing. This is observed both in SP and VP, but the amplitude of these peaks is smaller in VP. These local density peaks correspond to different streams in phase-space, where the SP and N-body velocities continue to agree.

- This process of shell crossing followed by a central peak followed by another shell crossing repeats multiple times, leading to more streams in phase space. After the second shell crossing, our N-body simulation starts developing spurious effects due to a relatively large softening length and small particle number. At later times, the phase space structure as seen in the SP solution contracts as the system approaches a steady state.

- The Husimi distribution approximates the Vlasov distribution, and we can calculate its moments directly from ψ. The calculation of velocity dispersion at the centre of the simulation box shows that it remains close to zero until shell crossing, after which it becomes large and shows oscillatory features. Thus, the SP equations offer a way to model CDM that remains valid after shell crossing, allows us to resolve multistreaming regions, and calculate all moments of the distribution function.

5.2 Outlook

We now make some comments on possible future work.

5.2.1 Improvements in 1D

A working direct Vlasov solver would allow us to make meaningful quantitative comparisons after the dust model breaks down. However, our VP solver is inaccurate and does not agree exactly with the other models. One possible reason is the lack of resolution in phase space. An approach to mitigate this is to employ an adaptive grid to allow better resolution in regions with high phase-space density. On a similar note, we would like to run an N-body simulation with more particles. This would make it possible to measure velocity dispersion in the simulation and compare to the measurement from SP. In the SP solver, $\hbar$ constrains phase-space resolution. To allow for better resolution at late times, we would like to use smaller values of $\hbar$. This necessitates the increase in the number of grid points to be used. We observe that the phase-space structure contracts at late times. To test whether the central structure reaches a steady state, we could verify the virial theorem in that region.

5.2.2 Extension to higher dimensions

Since we have worked in a 1D universe, a natural possibility is to extend our methods to either 2D or 3D and to simulate a more realistic universe. This extension comes with its own challenges. There are no exact analytical solutions in higher dimensions, and the computational costs will increase. The integrations of PT are nontrivial. Evolving the Vlasov distribution in 4D or 6D phase space is also a computational challenge, but numerical codes like `ColDICE` [83] which do the same already exist. The fact that the Schrödinger field ψ contains all relevant information and that we can build all higher moments from ψ is an advantage when extending to higher dimensions. In [57], this extension to 3D has already been tested for a modest box size, with a study of the systematic effects the SP equations might suffer from.

5.2.3 Extension to general cosmologies

Since we were interested in DM dynamics, we have worked in a DM only EdS universe. A possible next step could be to consider more general cosmologies, like a universe with nonzero vacuum energy. This can be done in a 3D universe, where a realistic power spectrum can be used to set up the initial conditions. The possibility of including mutliple fluids in the SP system was explored in [84], with analogy to multi-particle quantum systems.

5.2.4 Investigating the breakdown of PT

The PT expansion in the Eulerian picture was shown to fail *before* shell crossing in our toy universe. The question of when and how PT breaks down in a 3D universe with the standard cosmology is extremely interesting. Therefore, a systematic investigation of the failure of PT in a realistic universe is another possible research direction.

Bibliography

[1]   V. Springel, *The cosmological simulation code GADGET-2*,
      Monthly notices of the royal astronomical society **364** (2005) 1105 (cit. on pp. iii, 25, 38).

[2]   G. Van Rossum and F. L. Drake, *Python 3 Reference Manual*, CreateSpace, 2009,
      ISBN: 1441412697 (cit. on p. iii).

[3]   A. Einstein, *Die feldgleichungen der gravitation*,
      Sitzung der physikalische-mathematischen Klasse **25** (1915) 844 (cit. on p. 1).

[4]   K. Schwarzschild,
      Über das gravitationsfeld eines massenpunktes nach der einsteinschen theorie,
      SPAW (1916) 189 (cit. on p. 2).

[5]   J. Droste, *The field of a single centre in Einstein's theory of gravitation, and the motion of a
      particle in that field*, Ned. Acad. Wet., SA **19** (1917) 197 (cit. on p. 2).

[6]   J. T. Jebsen, *Über die allgemeinen kugelsymmetrischen Lösungen der Einstein'schen
      Gravitationsgleichungen im Vakuum*, Friedländer, 1921 (cit. on p. 2).

[7]   G. D. Birkhoff and R. E. Langer, *Relativity and modern physics*,
      Harvard University Press, 1923 (cit. on p. 2).

[8]   A. Friedmann,
      Über die Möglichkeit einer Welt mit konstanter negativer Krümmung des Raumes,
      Zeitschrift für Physik **21** (1924) 326 (cit. on p. 2).

[9]   G. Lemaître, *Expansion of the universe, A homogeneous universe of constant mass and
      increasing radius accounting for the radial velocity of extra-galactic nebulae*,
      Monthly Notices of the Royal Astronomical Society **91** (1931) 483 (cit. on p. 2).

[10] H. P. Robertson, *Kinematics and World-Structure*, The Astrophysical Journal **82** (1935) 284
      (cit. on p. 2).

[11] H. P. Robertson, *Kinematics and World-Structure II.*, The Astrophysical Journal **83** (1936) 187
      (cit. on p. 2).

[12] H. P. Robertson, *Kinematics and World-Structure III.*, The Astrophysical Journal **83** (1936) 257
      (cit. on p. 2).

[13] A. G. Walker, *On Milne's Theory of World-Structure*,
      Proceedings of the London Mathematical Society **42** (1937) 90 (cit. on p. 2).

[14] E. Hubble, *A relation between distance and radial velocity among extra-galactic nebulae*,
      Proceedings of the national academy of sciences **15** (1929) 168 (cit. on p. 2).

[15] A. G. Riess, *The expansion of the Universe is faster than expected*,
      Nature Reviews Physics **2** (2020) 10 (cit. on p. 2).

[16] M. J. Geller and J. P. Huchra, *Mapping the universe*, Science **246** (1989) 897 (cit. on p. 3).

[17] W. J. Percival et al.,
The 2dF Galaxy Redshift Survey: the power spectrum and the matter content of the Universe,
Monthly Notices of the Royal Astronomical Society **327** (2001) 1297 (cit. on p. 3).

[18] C. Stoughton et al., *Sloan digital sky survey: early data release*,
The Astronomical Journal **123** (2002) 485 (cit. on p. 3).

[19] A. Kogut et al., *Microwave emission at high galactic latitudes in the four-year DMR sky maps*,
The Astrophysical Journal Letters **464** (1996) L5 (cit. on p. 3).

[20] P. A. Ade et al., *Planck 2015 results-xiii. cosmological parameters*,
Astronomy & Astrophysics **594** (2016) A13 (cit. on pp. 3, 6).

[21] J. Ehlers, P. Geren and R. K. Sachs, *Isotropic Solutions of the Einstein-Liouville Equations*,
Journal of Mathematical Physics **9** (1968) 1344 (cit. on p. 3).

[22] W. R. Stoeger, R. Maartens and G. Ellis,
Proving almost-homogeneity of the universe: an almost Ehlers-Geren-Sachs theorem,
The Astrophysical Journal **443** (1995) 1 (cit. on p. 3).

[23] A. G. Riess et al., *Observational evidence from supernovae for an accelerating universe and a cosmological constant*, The Astronomical Journal **116** (1998) 1009 (cit. on p. 5).

[24] S. Perlmutter et al., *Measurements of Ω and Λ from 42 high-redshift supernovae*,
The Astrophysical Journal **517** (1999) 565 (cit. on p. 5).

[25] F. Zwicky, *Die rotverschiebung von extragalaktischen nebeln*,
Helvetica physica acta **6** (1933) 110 (cit. on p. 6).

[26] H. Andernach et al., *The Cluster M/L and the Value of Ω_m*,
arXiv preprint astro-ph/0407098 (2004) (cit. on p. 6).

[27] S. Weinberg et al., *Cosmology*, Oxford university press, 2008 (cit. on pp. 6, 65).

[28] V. C. Rubin, W. K. Ford Jr and N. Thonnard, *Rotational properties of 21 SC galaxies with a large range of luminosities and radii, from NGC 4605/R= 4kpc/to UGC 2885/R= 122 kpc*,
The Astrophysical Journal **238** (1980) 471 (cit. on p. 6).

[29] A. N. Taylor et al., *Gravitational Lens Magnification and the Mass of Abell 1689*,
The Astrophysical Journal **501** (1998) 539 (cit. on p. 6).

[30] S. Schindler, "Ω_M—Different Ways to Determine the Matter Density of the Universe",
Matter in the Universe, Springer, 2002 299 (cit. on p. 6).

[31] V. Sahni and P. Coles, *Approximation methods for non-linear gravitational clustering*,
Physics Reports **262** (1995) 1 (cit. on pp. 6, 13, 16, 18).

[32] G. R. Blumenthal et al., *Formation of galaxies and large-scale structure with cold dark matter*,
Nature **311** (1984) 517 (cit. on p. 7).

[33] M. McQuinn and M. White, *Cosmological perturbation theory in 1+ 1 dimensions*,
Journal of Cosmology and Astroparticle Physics **2016** (2016) 043 (cit. on pp. 7, 15, 17).

[34] A. Einstein and W. De Sitter,
On the relation between the expansion and the mean density of the universe, Proceedings of the
National Academy of Sciences of the United States of America **18** (1932) 213 (cit. on p. 7).

[35] L. D. Landau and E. M. Lifshitz, *Statistical Physics: Volume 5*, vol. 5, Elsevier, 2013 (cit. on p. 10).

[36] F. Bernardeau et al., *Large-scale structure of the Universe and cosmological perturbation theory*, Physics reports **367** (2002) 1 (cit. on pp. 11, 12, 14).

[37] N. Makino, M. Sasaki and Y. Suto, *Analytic approach to the perturbative expansion of nonlinear gravitational fluctuations in cosmological density and velocity fields*, Physical Review D **46** (1992) 585 (cit. on pp. 11, 14).

[38] G. K. Batchelor, *An Introduction to Fluid Dynamics*, Cambridge University Press, 1967 (cit. on p. 12).

[39] M. Goroff et al., *Coupling of modes of cosmological mass density fluctuations*, The Astrophysical Journal **311** (1986) 6 (cit. on pp. 12, 14).

[40] P. Schneider, *Cosmology Lecture Notes*, 2009 (cit. on p. 13).

[41] A. Meurer et al., *SymPy: symbolic computing in Python*, PeerJ Computer Science (2017) e103, ISSN: 2376-5992 (cit. on p. 16).

[42] Y. B. Zel'dovich, *Gravitational instability: An approximate theory for large density perturbations.*, Astronomy and astrophysics **5** (1970) 84 (cit. on p. 16).

[43] V. Arnold, S. Shandarin and Y. B. Zeldovich, *The large scale structure of the universe I. General properties. One-and two-dimensional models*, Geophysical & Astrophysical Fluid Dynamics **20** (1982) 111 (cit. on p. 17).

[44] S. N. Gurbatov, A. Saichev and S. Shandarin, *The large-scale structure of the universe in the frame of the model equation of non-linear diffusion*, Monthly Notices of the Royal Astronomical Society **236** (1989) 385 (cit. on p. 18).

[45] T. G. Brainerd, R. J. Scherrer and J. V. Villumsen, *Linear evolution of the gravitational potential: a new approximation for the nonlinear evolution of large-scale structure*, The Astrophysical Journal **418** (1993) 570 (cit. on p. 18).

[46] S. Matarrese et al., *A frozen-flow approximation to the evolution of large-scale structures in the Universe*, Monthly Notices of the Royal Astronomical Society **259** (1992) 437 (cit. on p. 18).

[47] D. Munshi and A. A. Starobinsky, *Non-Linear Approximations to Gravitational Instability: A Comparison in Second-Order Perturbation Theory*, arXiv preprint astro-ph/9311056 (1993) (cit. on p. 18).

[48] L. M. Widrow and N. Kaiser, *Using the Schrödinger equation to simulate collisionless matter*, The Astrophysical Journal **416** (1993) L71 (cit. on pp. 18, 19).

[49] D. Giulini and A. Großardt, *The Schrödinger–Newton equation as a non-relativistic limit of self-gravitating Klein–Gordon and Dirac fields*, Classical and Quantum Gravity **29** (2012) 215010 (cit. on p. 19).

[50] J. Rogel-Salazar, *The gross–pitaevskii equation and bose–einstein condensates*, European Journal of Physics **34** (2013) 247 (cit. on p. 19).

[51]   K. Takahashi, *Distribution functions in classical and quantum mechanics*,
       Progress of Theoretical Physics Supplement **98** (1989) 109 (cit. on pp. 19, 20).

[52]   G. Davies and L. M. Widrow,
       Test-bed simulations of collisionless, self-gravitating systems using the Schrödinger method,
       The Astrophysical Journal **485** (1997) 484 (cit. on p. 19).

[53]   M. Schaller et al., *A new framework for numerical simulations of structure formation*,
       Monthly Notices of the Royal Astronomical Society **442** (2014) 3073 (cit. on p. 19).

[54]   C. Uhlemann, M. Kopp and T. Haugg,
       Schrödinger method as N-body double and UV completion of dust,
       Physical Review D **90** (2014) 023517 (cit. on pp. 19, 21).

[55]   M. Garny and T. Konstandin, *Gravitational collapse in the Schrödinger-Poisson system*,
       Journal of Cosmology and Astroparticle Physics **2018** (2018) 009 (cit. on pp. 19, 35).

[56]   P. Mocz et al., *Schrödinger-Poisson–Vlasov-Poisson correspondence*,
       Physical Review D **97** (2018) 083519 (cit. on pp. 19, 20).

[57]   M. Garny, T. Konstandin and H. Rubira,
       The Schrödinger-Poisson method for Large-Scale Structure,
       Journal of Cosmology and Astroparticle Physics **2020** (2020) 003 (cit. on pp. 19, 37, 57).

[58]   C. Short and P. Coles, *Wave mechanics and the adhesion approximation*,
       Journal of Cosmology and Astroparticle Physics **2006** (2006) 016 (cit. on p. 19).

[59]   S. Pueblas and R. Scoccimarro,
       Generation of vorticity and velocity dispersion by orbit crossing,
       Physical Review D **80** (2009) 043504 (cit. on p. 19).

[60]   E. P. Wigner, "On the quantum correction for thermodynamic equilibrium",
       Part I: Physical Chemistry. Part II: Solid State Physics, Springer, 1997 110 (cit. on p. 19).

[61]   K. Husimi, *Some formal properties of the density matrix*,
       Proceedings of the Physico-Mathematical Society of Japan. 3rd Series **22** (1940) 264
       (cit. on p. 20).

[62]   R. T. Skodje, H. W. Rohrs and J. VanBuskirk,
       Flux analysis, the correspondence principle, and the structure of quantum phase space,
       Physical Review A **40** (1989) 2894 (cit. on p. 20).

[63]   M. Kopp, K. Vattis and C. Skordis,
       Solving the Vlasov equation in two spatial dimensions with the Schrödinger method,
       Physical Review D **96** (2017) 123532 (cit. on pp. 21, 22).

[64]   J. S. Bagla and T. Padmanabhan, *Cosmological N-body simulations*, Pramana **49** (1997) 161
       (cit. on pp. 24, 25).

[65]   G. Efstathiou et al., *Numerical techniques for large cosmological N-body simulations*,
       The Astrophysical Journal Supplement Series **57** (1985) 241 (cit. on p. 25).

[66]   R. Teyssier, *Cosmological hydrodynamics with adaptive mesh refinement-A new high
       resolution code called RAMSES*, Astronomy & Astrophysics **385** (2002) 337 (cit. on p. 25).

[67] A. V. Kravtsov, A. A. Klypin and A. M. Khokhlov,
Adaptive refinement tree: a new high-resolution N-body code for cosmological simulations,
The Astrophysical Journal Supplement Series **111** (1997) 73 (cit. on p. 25).

[68] E. Bertschinger, *Simulations of structure formation in the universe*,
Annual Review of Astronomy and Astrophysics **36** (1998) 599 (cit. on p. 25).

[69] J. W. Cooley and J. W. Tukey,
An algorithm for the machine calculation of complex Fourier series,
Mathematics of computation **19** (1965) 297 (cit. on p. 28).

[70] A. Iserles, *A first course in the numerical analysis of differential equations*, 44,
Cambridge university press, 2009 (cit. on p. 28).

[71] C. Cheng and G. Knorr, *The integration of the Vlasov equation in configuration space*,
Journal of Computational Physics **22** (1976) 330, ISSN: 0021-9991 (cit. on pp. 29, 31, 33).

[72] J. P. Boris and D. L. Book,
Flux-corrected transport. I. SHASTA, a fluid transport algorithm that works,
Journal of computational physics **11** (1973) 38 (cit. on p. 29).

[73] A. J. Klimas and W. M. Farrell,
A splitting algorithm for Vlasov simulation with filamentation filtration,
Journal of computational physics **110** (1994) 150 (cit. on p. 31).

[74] T. Utsumi, T. Kunugi and J. Koga,
A numerical method for solving the one-dimensional Vlasov—Poisson equation in phase space,
Computer physics communications **108** (1998) 159 (cit. on pp. 31, 33).

[75] M. Feit, J. Fleck Jr and A. Steiger, *Solution of the Schrödinger equation by a spectral method*,
Journal of Computational Physics **47** (1982) 412 (cit. on p. 35).

[76] D. Kosloff and R. Kosloff, *A Fourier method solution for the time dependent Schrödinger equation as a tool in molecular dynamics*, Journal of Computational Physics **52** (1983) 35
(cit. on p. 35).

[77] D. J. Tannor, *Introduction to quantum mechanics: a time-dependent perspective*,
University Science Books, 2007 (cit. on p. 35).

[78] J. Izaac and J. Wang, *Computational quantum mechanics*, Springer, 2018 (cit. on p. 35).

[79] G. B. Arfken and H. J. Weber, *Mathematical methods for physicists*,
American Association of Physics Teachers, 1999 (cit. on p. 37).

[80] M. Michaux et al., *Accurate initial conditions for cosmological N-body simulations: Minimizing truncation and discreteness errors*,
Monthly Notices of the Royal Astronomical Society **500** (2020) 663 (cit. on p. 39).

[81] V. Springel, *User guide for GADGET-2*,
Max-Plank-Institute for Astrophysics, Garching, Germany (2005) (cit. on p. 39).

[82] C. Rampf and O. Hahn, *Shell-crossing in a {\Lambda} CDM Universe*,
arXiv preprint arXiv:2010.12584 (2020) (cit. on p. 46).

[83]   T. Sousbie and S. Colombi,
       ColDICE: A parallel Vlasov–Poisson solver using moving adaptive simplicial tessellation,
       Journal of Computational Physics **321** (2016) 644 (cit. on p. 57).

[84]   R. Johnston, A. Lasenby and M. Hobson,
       Cosmological fluid dynamics in the Schrödinger formalism,
       Monthly Notices of the Royal Astronomical Society **402** (2010) 2491 (cit. on p. 57).

Calculation of $G_{\mu\nu}$ for a flat FLRW metric

We start by calculating the Christoffel symbols (Γ's), which can be expressed in terms of the metric and its partial derivatives [27]

$$\Gamma^{\sigma}_{\mu\nu} = \frac{1}{2} g^{\sigma\rho} \left(\frac{\partial g_{\nu\rho}}{\partial x^{\mu}} + \frac{\partial g_{\rho\mu}}{\partial x^{\nu}} - \frac{\partial g_{\mu\nu}}{\partial x^{\rho}} \right) . \tag{A.1}$$

The flat FLRW metric is

$$\mathrm{d}s^2_{\mathrm{FLRW}} = c^2 \, \mathrm{d}t^2 - a^2(t) \left\{ \mathrm{d}r^2 + r^2 \left[\mathrm{d}\theta^2 + \sin^2(\theta) \, \mathrm{d}\phi^2 \right] \right\} . \tag{A.2}$$

The metric is diagonal, its 00 component is constant, and the remaining components are only time dependent. These symmetries of the metric carry over to the Christoffel symbols and the Ricci tensor. First, we note that all Γ^{i}_{jk} vanish if two of (i, j, k) are zero. Further, the symbols are symmetric in their lower two indices ($\Gamma^{i}_{jk} = \Gamma^{i}_{kj}$). This leaves us with only a few unique nonzero symbols. They are as follows

$$\Gamma^0_{11} = \frac{a\dot{a}}{c} , \qquad \Gamma^0_{22} = \frac{a\dot{a}r^2}{c} , \qquad \Gamma^0_{33} = \frac{a\dot{a}r^2 \sin^2(\theta)}{c} ,$$

$$\Gamma^1_{22} = -r , \qquad \Gamma^2_{12} = \Gamma^3_{13} = \frac{1}{r} , \qquad \Gamma^1_{33} = -r\sin^2(\theta) , \tag{A.3}$$

$$\Gamma^i_{0i} = \frac{c\dot{a}}{a} , \qquad \Gamma^2_{33} = \sin(\theta)\cos(\theta) , \qquad \Gamma^3_{23} = \cot(\theta) .$$

We have the following formula for the Ricci tensor [27]

$$R_{\mu\nu} = \frac{\partial \Gamma^{\lambda}_{\lambda\mu}}{\partial x^{\nu}} - \frac{\partial \Gamma^{\lambda}_{\mu\nu}}{\partial x^{\lambda}} + \Gamma^{\lambda}_{\mu\sigma}\Gamma^{\sigma}_{\nu\lambda} - \Gamma^{\lambda}_{\mu\nu}\Gamma^{\sigma}_{\lambda\sigma} . \tag{A.4}$$

Isotropy of the metric ensures that R_{i0} and R_{0j} both vanish. The Ricci tensor is thus diagonal, and the all the components can be expressed as

$$R_{00} = 3\frac{\ddot{a}}{ac^2} , \tag{A.5a}$$

$$R_{11} = -\left(\frac{a\ddot{a} + 2\dot{a}^2}{c^2}\right) , \tag{A.5b}$$

$$R_{22} = -\left(\frac{a\ddot{a} + 2\dot{a}^2}{c^2}\right) r^2 , \tag{A.5c}$$

$$R_{33} = -\left(\frac{a\ddot{a} + 2\dot{a}^2}{c^2}\right) r^2 \sin^2(\theta) . \tag{A.5d}$$

We can now construct the Ricci scalar R as

$$R = g^{\mu\nu} R_{\mu\nu} , \tag{A.6}$$

which gives

$$R = \frac{6}{c^2}\left[\frac{\ddot{a}}{a} + \left(\frac{\dot{a}}{a}\right)^2\right] . \tag{A.7}$$

Finally, we combine Eq. (A.5) and Eq. (A.7) to obtain the Einstein tensor

$$G_{\mu\nu} = R_{\mu\nu} - \frac{1}{2}R g_{\mu\nu} , \tag{A.8}$$

$$G_{00} = -3\left(\frac{\dot{a}}{ac}\right)^2 , \tag{A.9a}$$

$$G_{ii} = \frac{2\ddot{a}a + \dot{a}^2}{c^2} . \tag{A.9b}$$